AD-A047 485 PITTSBURGH UNIV PA DEPT OF METALLURGICAL AND MATERI--ETC F/G 11/6
EFFECT OF SOLUTE REDISTRIBUTION ON THE STRUCTURE AND PROPERTIES--ETC(U)
OCT 77 S A DAVID, J MATHEW, H D BRODY N00014-75-C-0800
UNCLASSIFIED SETEC-MME-77-110 NL

| OF |
AD
A047485

END
DATE
FILMED
1 -78
DDC

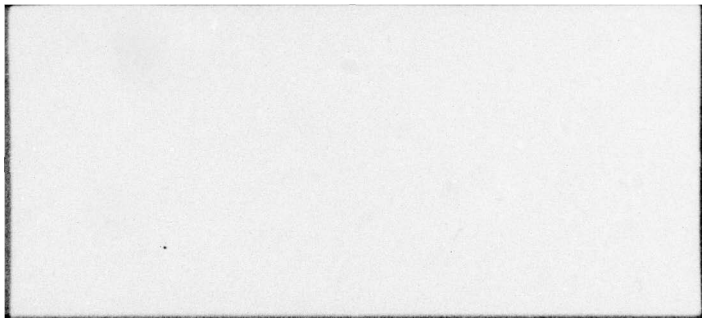

SETEC-MME-77-110

(1)

EFFECT OF SOLUTE REDISTRIBUTION ON THE STRUCTURE AND PROPERTIES OF CAST ALLOYS: PERITECTIC SOLIDIFICATION AND MODEL OF CONTINUOUS CASTING

S. A. David, J. Mathew, and H. D. Brody

ONR CONTRACT N00014-75-C-0800

Technical Report

October 1977

SECURITY CLASSIFICATION OF THIS PAGE (When Data Entered)

REPORT DOCUMENTATION PAGE

READ INSTRUCTIONS BEFORE COMPLETING FORM

1. REPORT NUMBER
2. GOVT ACCESSION NO.
3. RECIPIENT'S CATALOG NUMBER

4. TITLE (and Subtitle)
(6) Effect of Solute Redistribution on the Structure and Properties of Cast Alloys: Peritectic Solidification and Model of Continuous Casting.

5. TYPE OF REPORT & PERIOD COVERED
(9) Technical Report,

6. PERFORMING ORG. REPORT NUMBER
(14) SETEC-MME-77-110

7. AUTHOR(s)
(10) S. A./David, J./Mathew/ [redacted] H. D./Brody

8. CONTRACT OR GRANT NUMBER(s)
(15) N00014-75-C-0800

9. PERFORMING ORGANIZATION NAME AND ADDRESS
Department of Metallurgical and Materials Engineering, University of Pittsburgh
Pittsburgh, Pennsylvania 15261

10. PROGRAM ELEMENT, PROJECT, TASK AREA & WORK UNIT NUMBERS

11. CONTROLLING OFFICE NAME AND ADDRESS
(11) Metallurgy Program, Office of Naval Research
800 N. Quincy
Arlington, Virginia 22217

12. REPORT DATE
Oct [redacted] 77 (12)

13. NUMBER OF PAGES
54 p.

14. MONITORING AGENCY NAME & ADDRESS(if different from Controlling Office)

15. SECURITY CLASS. (of this report)

15a. DECLASSIFICATION/DOWNGRADING SCHEDULE

16. DISTRIBUTION STATEMENT (of this Report)

DISTRIBUTION STATEMENT A
Approved for public release;
Distribution Unlimited

17. DISTRIBUTION STATEMENT (of the abstract entered in Block 20, if different from Report)

402 241

18. SUPPLEMENTARY NOTES

19. KEY WORDS (Continue on reverse side if necessary and identify by block number)

solidification	metastable phases	continuous casting
peritectics	lead alloys	heat flow
composites	tin alloys	stress analysis
	aluminum alloys	computer simulations

20. ABSTRACT (Continue on reverse side if necessary and identify by block number)

Two papers presented at the Sheffield International Symposium on Solidification are included. One paper covers a theory to describe the relation between casting conditions and structure in directionally solidified peritectic alloys. Experiments on Pb-Bi and Sn-Cd alloys are used to check the theory. The second paper describes the application of a computer model of continuous casting to study the effects of ingot diameter and casting rate on heat flow and thermal stresses in an aluminum-magnesium alloy.

DD FORM 1 JAN 73 1473 EDITION OF 1 NOV 65 IS OBSOLETE
S/N 0102-014-6601

SECURITY CLASSIFICATION OF THIS PAGE (When Data Entered)

CONTROLLED SOLIDIFICATION OF PERITECTIC ALLOYS

H. D. Brody and S. A. David
Department of Metallurgical and Materials Engineering
848 Benedum Hall
University of Pittsburgh
Pittsburgh, PA 15261 U.S.A.

Synopsis

Pb-Bi and Sn-Cd as models of alloys from peritectic systems have been directionally solidified under controlled conditions for moderate and high values of G/R. A variety of microstructures have been obtained. Alloys which would solidify as two phases under equilibrium conditions, when solidified under conditions of plane front growth at high values of G/R, formed single phase metastable solid solutions of the peritectic product phase. At moderate values of G/R the alloys have been grown with well aligned two phase morphologies. However, because growth of the two solid phases is not coupled, the spacing between phases is much coarser than in eutectic systems.
An analysis of the growth conditions that lead to the observed microstructures is presented.

In recent years controlled solidification of peritectic alloys has been receiving a great deal of attention and has been a subject of detailed analytical and experimental studies.[1-5] Much of the recent work was aimed at resolving the several conflicting hypotehses that have been put forth as to the structures expected on directional solidification of peritectic alloys.[6-8] Several authors have discussed the directional freezing of peritectic alloys under the conditions of small values of the temperature gradient/growth rate ratio (G/R).[6,9] However initial results on directional freezing of peritectic alloys under conditions of moderate and high values of G/R have produced surprising results that are not in complete agreement with the existing hypotheses.[5]

For an alloy of composition C_0 between the compositions above pure A and up to C_L in the peritectic phase diagram of Figure 1, the freezing process for small G/R may be described, schematically, as in Figure 2. The temperature gradient is shown in Figure 2a where x_t, x_p, and x_r represent the instantaneous positions of the liquidus, peritectic, and effective solidus isotherms. The effective solidus, as shown in Figure 1, is the temperature where the last liquid, C_L^f, freezes as the average composition of the cored, often two phase solid reaches C_0. In line with previous studies,[10-11] the assumptions are made that the liquid is uniform in composition along an isotherm, equilibrium applies to the solid/liquid interface,* and that there is negligible undercooling before nucleation of solid phases. Then solid plus liquid coexist between x_t and x_r and the liquidus curve may be used to generate the curve of solute distribution in the liquid within the solid plus liquid

*The equilibrium interface compositions are given by the equilibrium partition ratio, $K=C_S^*/C_L^*$, where C_S^* and C_L^* are the solid and liquid compositions given by the tie line at the temperature of a particular location. Herein K_1 refers to the equilibrium between S_1 and L and K_2 to equilibrium between S_2 and L.

zone, Figure 2b. For low values of G/R the assumption has been made that diffusion across the mushy zone is negligible and the tips of the dendrites are not undercooled due to either constitutional or kinetic effects.[10,12-14] If, for simplicity in sketching, the dendrites are considered to be plates, Figure 2c represents the distribution of phases. S_2 first nucleates at the peritectic temperature and quickly envelopes S_1. From the point of complete envlopment two phase equilibrium is maintained at two interfaces, S_2/L and S_1/S_2. In some systems S_2 has been found to nucleate and grow epitaxially on S_1.[15] In other systems S_2 has been reported to nucleate heterogeneously in the liquid and then to grow together until it surrounds S_1.[2] In directional freezing, nucleation of S_2 near T_p is not considered to be a difficulty due to the presence of previously grown S_2 in regions of lower temperature. Figure 2d shows a volume element taken between two dendrite arms at a time when the element is at a temperature below T_p and above T'_S. At the L/S_2 interface S_2 forms by solidification with concomitant rejection of solute at the interface and an increase in the liquid composition, e.g. at T'

$$L(C'_L) \rightarrow S_2(C'_{2L}) + \text{solute } [B] \quad \ldots\ldots(1)$$

Diffusion occurs across the S_2 rim due to the composition gradient in the S_2 as shown in Figure 2e. The difference $(C'_{2L}-C'_2)$ increases as the temperature decreases below the peritectic temperature. As a result of this diffusion flux solute is brought to the S_1/S_2 interface. At the latter interface solute is incorporated by the transformation of S_1 to S_2, e.g. at T'

$$S_1(C'_1) + \text{solute } [B] \rightarrow S_2(C'_2) \quad \ldots\ldots(2)$$

It is by the combination of these two reactions that the peritectic transformation proceeds

$$L + S_1 \rightarrow S_2 \quad \ldots\ldots(3)$$

However, the ratio of L and S_1 that are consumed is not fixed by the phase diagram, but is determined by the extent of diffusion through the S_2 rim. In

the limit of the case of negligible diffusion in S_2 during freezing, no S_1 would be consumed, freezing would not be complete until the volume element reached the melting point of B, and the last solid to form would be pure B.

As the temperature gradient/growth rate ratio is increased, the diffusion flux along the concentration gradient in the liquid, Figure 2b, increases and the temperature of the dendrite tips, T_t, is lowered below the equilibrium liquidus, T_L, by an amount of ΔT which is given approximately by[10-13]

$$\Delta T = T_L - T_t = \frac{D_L G}{R} \quad \ldots\ldots(4)$$

where D_L is the diffusion coefficient of the solute in the liquid. Thus, S_1 first forms at a lower temperature and the composition of the first S_1 to form is increased above $K_1 C_0$ according to the solidus curve. Also it is more likely that as G/R increases, the dendrites will become simpler in morphology and eventually side branches will not form. (An unbranched rod interface would be termed cellular by Flemings.[12]) At a sufficiently high value of G/R the constitutional undercooling will be sufficient to suppress the dendrite tip temperature to the equilibrium solidus. For compositions between pure A and C_1, this condition is the same as that for plane front growth of S_1

$$G/R \geq \frac{m_1 C_0 (1-K_1)}{D_L K_1} \quad \ldots\ldots(5)$$

where m_1 (defined positive) is the slope of the liquidus curve for S_1 at $C_L = C_0/K_1$. This constitutional supercooling criterion for plane front freezing of S_1 is plotted as $\overline{oa}$ in Figure 3.

The condition for suppressing the S_1 dendrite tips below the peritectic temperature, which is the equilibrium solidus for compositions between C_1 and C_2 is given by

$$G/R \geq \frac{m_1 (C_L - C_0)}{D_L} \quad \ldots\ldots(6)$$

This relation is plotted as $\overline{abd}$ in Figure 3.

As the diffusion flux across the mushy zone causes an increase in the solute concentration of the dendrite tips, it also causes a decrease in solute concentration of the liquid at the end of freezing. For compositions above C_2, a planar S_2/L interface will result when the composition at the dendrite roots is C_0/K_2 and T_s' equals the equilibrium solidus temperature as in the constitutional supercooling criterion written for S_2

$$G/R \geq \frac{m_2 C_0}{D_L} \frac{(1-k_2)}{k_2} \quad \text{.....(7)}$$

where m_2 (defined positive) is the slope of the liquidus curve for S_2 at $C_L=C_L^f$. For compositions between pure A and C_2 a planar interface between S_2 and L can be achieved when values for the metastable extension of the S_2 liquidus and solidus are substituted in criterion (7). In this region the S_2/L interface would be at a temperature higher than the peritectic temperature. This criterion is plotted as $\overline{obc}$ in Figure 3.

Region A represents the normal freezing conditions at small values of G/R. Here, dendrites of the primary phase, S_1, would grow ahead of the peritectic isotherm and be surrounded by gradually thickening S_2 below the peritectic isotherm, as sketched in Figure 2. For higher values of G/R in region B, primary dendrites or cells of S_1 will grow with higher undercoolings at the tips and S_2 will freeze at a plane front at the peritectic temperature. For higher initial solute contents, in region C, S_2 will grow with either a dendritic or cellular interface. For still higher values of G/R in region D and E, single phase material will grow at a plane front. For low solute contents in region D, S_1 will grow. For higher solute contents in region E, S_2 will form. For compositions between C_1 and C_2 at values of G/R in region E, single phase S_2 will grow at the metastable S_2 solidus even though two phases would be stable. Since the metastable solidus is higher than the peritectic temperature, the requirement for suppressing the formation of S_1 would not be given by criterion (6) but would fall on a line slightly below $\overline{ab}$ in Figure 3.

For simplicity of presentation, the revised criterion is not shown.

Figure 3 represents, substantially, the initial growth forms under the assumptions listed above, namely,

no undercooling due to kinetic or curvature effects

equilibrium at all solid/liquid interfaces

no undercooling before nucleation of solid phases

perfect mixing in the liquid along any isothermal surface.

However, the structure that first forms would not be a final equilibrium structure and so changes in structure might occur before the end of freezing. For example, in regions A and B up to initial solute contents of C_1 single phase S_1 would be the equilibrium product of solidification. Diffusion in S_1 during freezing would result in reduction in the extent of coring in primary S_1 and a reduction in the amount of S_2 that formed.[10] For substantial diffusion in S_1 during freezing, S_2 would not form. Similarly in region A, S_1 will tend to convert to S_2 by reaction (2) as a result of diffusion through the rim of S_2. The interface between S_1 and S_2 might move first in one direction then another due to the difference in diffusion rate within S_1 and S_2 and the slopes of the solvus lines.

In region E for compositions between C_1 and C_2 single phase S_2 would form at the metastable solidus temperature, which would be above the peritectic temperature. After forming, the S_2 would cool through two regions of two phase equilibrium, S_1+L and then S_1+S_2, where the latter is the equilibrium phase distribution. If S_1 is slow to nucleate and/or diffusion in the solid is sluggish, metastable S_2 expected after freezing would persist to room temperature. If S_1 were to nucleate and grow sufficiently below the peritectic temperature no interference with the liquid/solid interface would occur. However, if S_1 nucleated close to the interface and diffusion were rapid, the metastable S_2/L interface could shift to an equilibrium S_1/L interface which would be cellular or dendritic at these conditions.

Experimental

Alloys from the Pb-Bi and Sn-Cd system were directionally solidified at a variety of G/R values to establish the growth conditions for peritectic systems in which diffusion in the solid phases is relatively slow. All samples were made from pure metals with initial purities greater than 99.99%. Rods of the desired composition were formed by first melting an alloy of composition C_0 in a crucible, and drawing the molten alloy into a pyrex tube by means of a partial vacuum. Before drawing the sample, a 100 micron chromel-alumel thermocouple in a 0.1 cm double bore mullite protection tube was inserted in the Pyrex tube. The thermocouple tip was coated with boron nitride slurry.

Samples were placed in a vertical resistance zone melting and freezing apparatus sketched in Figure 4. The distance between the heating element and the following chills was set at 0.5 cm. Gradients of up to 360°C/cm and 340°C/cm were achieved in Pb-Bi and Sn-Cd, respectively. At least one zone melting pass was made before the final directional freezing pass. In the last pass the solid/liquid interface was quenched by switching off the power to the heater and increasing the water flow through the chills. Due to the highly oxidizing nature of the Pb-Bi alloys a special polishing technique involving a combination of mechanical and electropolishing techniques was developed and used. The electrolyte consists of 40 ml of glycerol, 10 ml of acetic acid, and 10 ml of nitric acid. Sn-Cd samples were polished to 0.01 micron alumina and etched with a solution containing 5 ml of nitric acid and 95 ml of lactic acid.

Pb-Bi System

As indicated in the phase diagram for Pb-Bi, Figure 5, the peritectic reaction at 184°C is

$$(23.3\%Bi) + L(36\%Bi) \longrightarrow (33\%Bi) \quad \ldots\ldots\ldots\ldots\ldots\ldots\ldots\ldots\ldots\ldots (8)$$

Samples were directionally solidified in the zone refining apparatus with bismuth compositions ranging from 24 to 35 weight percent and for values of

G/R ranging from 0.48×10^6 to 4.58×10^6 ^{o}C sec cm^{-2}. Table 1 lists the samples made and the microstructural observations. Figure 6 illustrates the range of microstructures observed. Photomicrographs at the bottom are of transverse sections, perpendicular to heat flow. Photomicrographs at the top are of longitudinal sections, parallel to heat flow. The longitudinal sections were taken at the position of the quenched solid/liquid interface.

At low values of G/R, Figure 6a, the α phase leads the β phase. The dendrites are branched and are seen to be highly plate like at low values of G/R, note Figure 7. At higher values of G/R, Figure 6b, the α phase still leads the β, but the rods of α are not branched and the β appears to form at a plane front. However, the latter observation is tenuous. If there were a liquid groove extending below the region where β first forms, it would not be readily seen as the liquid and β in this system are nearly the same composition, i.e. $k_2 \sim 1$. In the transverse section the structure is similar to a directionally solidified eutectic, except that the spacing is coarser. The spacing between the rods of α is 60 microns. At high values of G/R, Figure 6c, the α rods are completely suppressed and β grows at a plane front. If the conditions are close but not sufficient for a planar β/L interface to be stable, a cellular interface develops as in Figure 8.

Figure 9 summarizes the results for Pb-Bi. Lines representing the criteria in equations (5) to (7) are drawn on Figure 9. These lines are surprisingly good fits for the boundaries separating the morphological behavior of the alloys.

If the solidification behavior of Pb-Bi is in line with the theory presented previously, then the temperature of the β/L interface for conditions of single phase growth at compositions between 24 and 33% Bi should be above the peritectic temperature. Two experiments were run to determine the interface temperature. In each rod two thermocouples were inserted at a distance of 0.5 cm

apart. The sample was directionally solidified until the bottom thermocouple indicated a temperature below the peritectic. Then the sample was quenched. The distance of the interface from both thermocouples was measured and the temperature of the interface estimated by assuming a linear temperature gradient in the region of the two thermocouples. The temperatures measured for Pb-28%Bi and Pb-30%Bi alloys were on a line that is consistent with the metastable extension of the β solidus. These points are plotted as (1) and (2) in Figure 5.

Sn-Cd System

As indicated in the phase diagram for Sn-Cd, Figure 10, the peritectic reaction at 221°C is reported[17] as

$$\varepsilon(0.75\%Cd) + L(3.8\%Cd) \rightarrow \delta(2.1\%Cd) \quad \ldots\ldots\ldots\ldots\ldots\ldots\ldots\ldots\ldots\ldots (9)$$

Samples were directionally solidified in the zone melting and freezing apparatus with cadmium compositions ranging from 1.0 to 1.75 weight percent and for values of G/R ranging from 0.5×10^5 to 1.5×10^6 °C sec cm^{-2}. Table 2 lists the experiments run and the microstructural observations. The range of microstructures observed in Sn-Cd was similar to Pb-Bi with one major additional microstructural feature. Figure 11 indicates the range of microstructures that parallel Pb-Bi. Figure 11a shows the composite like microstructure obtained at moderate values of G/R as rods of ε lead what appears to be a planar interface of δ . At high values of G/R single phase δ grows at a planar interface. Additionally, some samples at high values of G/R exhibited a banded structure Figures 12 and 13. The bands generally alternate between ε and δ and run transverse to the growth direction, parallel to the isotherms. On occasion a band will consist of ε and δ growing side by side.

In Figure 14 the results for Sn-Cd are summarized. The results of Boettinger[1] are also plotted in Figure 14. With the exception of the region of banding the results are consistent with the theory presented earlier. The

lines based on the criteria of equations (5) to (7) are not in as good agreement with the boundaries of morphological behavior as was the case for Pb-Bi.

The banding phenomenon may have several sources. One explanation would be that the δ/L interface which might be expected would be disrupted by nucleation of ϵ behind the interface. This ϵ would grow up to the interface and grow for a short time until the solute builds up to a point to again nucleate δ. This process repeats every time ϵ is nucleated at high temperature. For higher values of G/R banding is extinguished. This can be explained because the solidified δ cools more quickly to a temperature where ϵ will not nucleate due to the higher temperature gradients.

Summary

A theory has been proposed and experiments with Pb-Bi and Sn-Cd have given reasonable confirmation that peritectic alloys can be directionally solidified to give a variety of microstructures.

1. At low values of G/R, branched dendrites of the pro-peritectic phase will be surrounded below the peritectic isotherm by the peritectic product phase.

2. At moderate values of G/R, simple growth forms (such as rods) of the pro-peritectic phase grow with high undercooling ahead of a planar interface of the peritectic product phase. The structure resembles a eutectic composite except it is coarser.

3. At high values of G/R, formation of the pro-peritectic phase is suppressed and the peritectic product phase grows at a plane front. For those compositions that would be two phase according to the equilibrium phase diagram, the temperature of the planar interface is above the peritectic temperature and is the temperature on the metastable extension of the solidus of the peritectic product phase. The phase that forms will be metastable (supersaturated with solvent, for $k \ll 1$). The planar interface can be disrupted by nucleation of the pro-peritectic phase behind the interface.

Acknowledgements

The authors wish to thank Dr. G. I. Scherbakov for his contribution during the initial stages of this investigation. The authors are grateful to the Office of Naval Research (ONR Contract N00014-67-A-0402-0003) for support of this work.

References

1. Boettinger, W. J., Met. Trans. 1974, vol. 5, pp. 2023-31.
2. Baker, N. J. W. and Hellawell, A., Metal Science, 1974, vol. 8, pp. 353-56.
3. Titchener, A. P. and Spittle, J. A., Acta Met., 1975, vol. 23, pp. 297-502.
4. St. John, D. H. and Hogan, L. M., Acta Met., 1977, pp. 77-81.
5. Scherbakov, G. I., David, S. A. and Brody, H. D., Scripta Met. 1974, vol. 8, pp. 1239-43.
6. Uhlmann, D. R. and Chadwick, B. A., Acta Met., 1961, vol. 9, pp. 835-43.
7. Chalmers, B., Physical Metallurgy, p. 271, 1959, New York, John Wiley and Sons.
8. Flemings, M. C., Solidification Processing, p. 117, 1974, New York, McGraw-Hill Book Company.
9. Sartell, J. A. and Mack, D. J., J. Inst. of Metals, 1964, vol. 93, pp. 19-24.
10. Brody, H. D. and Flemings, M. C., Trans A.I.M.E., 1966, vol. 236, pp. 615-24.
11. Bower, T. F., Brody, H. D. and Flemings, M. C., Trans. A.I.M.E., 1966, vol. 236, pp. 624-34.
12. Flemings, M. C., Solidification Processing, Chapter 3, 1974, New York, McGraw-Hill Book Company.
13. Sharp, R. M. and Flemings, M. C., Met. Trans., 1974, vol. 5, pp. 823-30.
14. Sharp, R. M. and Flemings, M. C., Met. Trans., 1973, vol. 4, pp. 997-01.
15. Greninger, Trans. Amer. Inst. Min. Met. Eng., 1937, vol. 124, pp. 379-81.

16. Hansen, M. and Anderko, K., Constitution of Binary Alloys, 1958, New York, McGraw-Hill Book Company.

17. Pell-Walpole, W. T., Metals Handbook, p. 1189, 1948, ASM, Cleveland.

Table 1

Composition, Growth Conditions and Observed Microstructures in Pb-Bi Alloys

C_o wt pct Bi	G °C per cm	R cm per sec x 10^4	G/R °C x sec per cm^2 x 10^{-6}	Structure	Quenched S/L interface shape
24	220	4.58	0.48	$\alpha+\beta$	Branched α dendrite leading
24	244	2.83	0.86	$\alpha+\beta$	Rods of α leading
24	298	1.39	2.1	$\alpha+\beta$	Rods of α leading
26	250	3.47	0.72	$\alpha+\beta$	Branched α dendrite leading
26	360	2.83	1.27	$\alpha+\beta$	Rods of α leading
26	350	2.22	1.57	$\alpha+\beta$	Rods of α leading
26	255	1.39	1.84	$\alpha+\beta$	Rods of α leading
26	275	1.39	1.98	$\alpha+\beta$	Rods of α leading
28	200	1.94	1.03	$\alpha+\beta$	Branched α dendrite leading
28	260	1.66	1.55	$\alpha+\beta$	Rods of α leading
28	338	0.83	4.87	β	Plane front β
30	230	4.58	0.50	$\alpha+\beta$	Rods of α leading
30	283	4.39	0.64	$\alpha+\beta$	Rods of α leading
30	283	1.67	1.70	$\alpha+\beta$	Rough interface
30	220	1.02	2.17	β	Plane front β
30	226	0.83	2.72	β	Plane front β
32	277	4.58	0.60	$\alpha+\beta$	Rods of α leading
32	225	1.39	1.60	β	Cells of β
32	275	1.39	1.98	β	Plane front β
33	152	5.55	0.27	$\alpha+\beta$	Rods of α leading
33	195	4.17	0.47	$\alpha+\beta$	Rods of α leading
33	258	1.39	1.86	β	Plane front β
33	266	2.22	1.20	β	Cells of β
35	354	5.55	0.64	β	Cells of β
35	340	4.58	0.71	β	Cells of β
35	255	3.06	1.10	β	Cells of β

LIST OF FIGURES

Table 2

Composition, Growth Conditions and Observed Microstructures in Sn-Cd Alloys

C_o wt pct Cd	G °C per cm	R cm per sec x 10^4	G/R °C x sec per cm^2 x 10^{-5}	Structure	Quenched S/L Interface Shape
1.0	241	16.66	1.45	ε + δ	Rods of ε leading
1.0	230	8.33	2.76	Banded ε and δ	---
1.0	200	4.58	4.30	Banded ε and δ	---
1.0	152	2.22	6.84	Banded ε and δ	---
1.5	152	16.66	0.90	ε + δ	Rods of ε leading
1.5	234	11.11	2.10	Banded ε and δ	---
1.5	150	4.58	2.76	Banded ε and δ	---
1.5	143	1.39	10.30	δ	Plane front δ
1.5	340	2.70	12.2	δ	Plane front δ
1.75	82	16.66	0.49	δ	Cells of δ
1.75	251	26.28	0.95	δ	Cells of δ
1.75	127	4.58	1.52	δ	Cells of δ
1.75	95	4.58	2.10	δ	Cells of δ
1.75	179	3.47	5.20	δ	Plane front δ

Figure Legends

Figure 1. Binary peritectic phase diagram.

Figure 2. Model for directional solidification of peritectic alloys a). Temperature distribution during unidirectional solidification b). Liquid composition in the solid and liquid and in the liquid region c). Illustration of the sequence of formation of solid phases indicating position of the characteristic volume element d). Sketch of a volume element considered in the solid and liquid region e). Concentration profile along the length of the volume element.

Figure 3. Critical G/R vs Co plot to obtain planar solid-liquid interface, as defined by equations 5-7. Also shown are the expected microstructures and interface morphology.

Figure 4. A low temperature vertical zone melting unit showing the heating and cooling arrangements.

Figure 5. Constitution diagram of Pb-Bi system[16] with extended metastable solidus. Data points represent the actual interface temperatures measured at the solid (plane front β)/liquid interface.

Figure 6. Typical aligned structures showing the effect of G/R ratios. In each case the top photomicrograph is a longitudinal section including the quenched interface, and the bottom is a transverse section. (a) Co=28wt% Bi; G/R=1.03×10^{6}°C-sec. per cm^2, (b) Co=28 wt% Bi; G/R=1.55×10^{6}°C-sec per cm^2, (c) Co=28 wt% Bi; G/R=4.87×10^{6}°C-sec per cm^2 (50X).

Figure 7. Three dimensional composite photomicrograph showing branched plate-like dendrites of α phase surrounded by β phase.

Figure 8. Photomicrograph of a quenched interface which is cellular β. (100X)

Figure 9. Structures of directionally solidified Pb-Bi alloys and interface shapes as a function of G/R and C_o.

Figure 10. Constitution diagram of Sn-Cd system.[17]

Figure 11. Typical longitudinal and transverse photomicrographs showing the effect of G/R ratios. (a) Co=1.5 wt% Cd; G/R=0.9×10^{5}°C-sec per cm^2 (b) Co=1.5 wt% Cd; G/R=1.03×10^{6}°C-sec per cm^2 (100X).

Figure 12. a) Photomicrograph of a longitudinal section including the quenched interface showing ε phase nucleating and growing along with δ phase without any interference with the planar solid-liquid interface.
b) Transverse photomicrograph of the same sample.

Figure 13. Banding in directionally solidified Sn-Cd alloys. a) Photomacrograph of directionally solidified sample (2X). b) Photomicrograph of the same sample showing alternate layers of ε and δ (50X).

Figure 14. Structures of directionally solidified Sn-Cd alloys and interface shapes as a function of G/R and C_o.

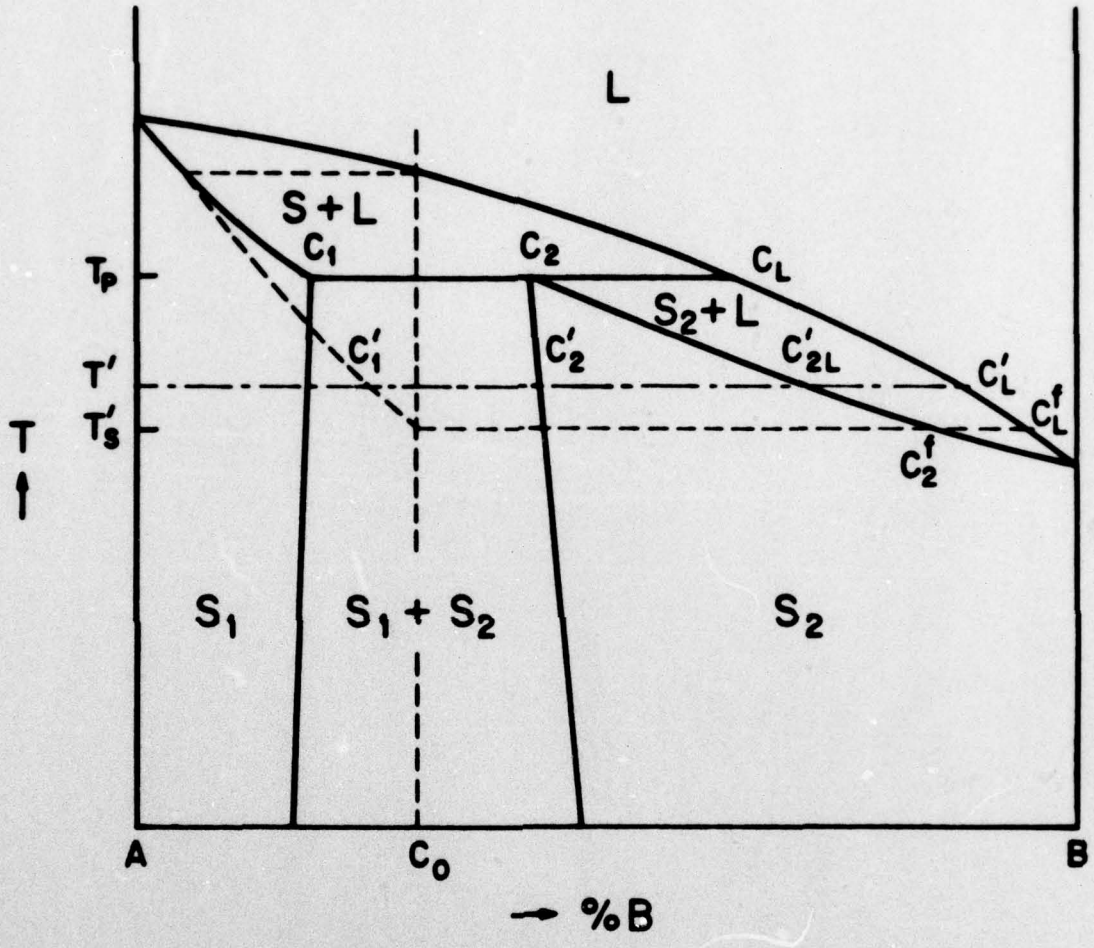

Figure 1. Binary peritectic phase diagram.

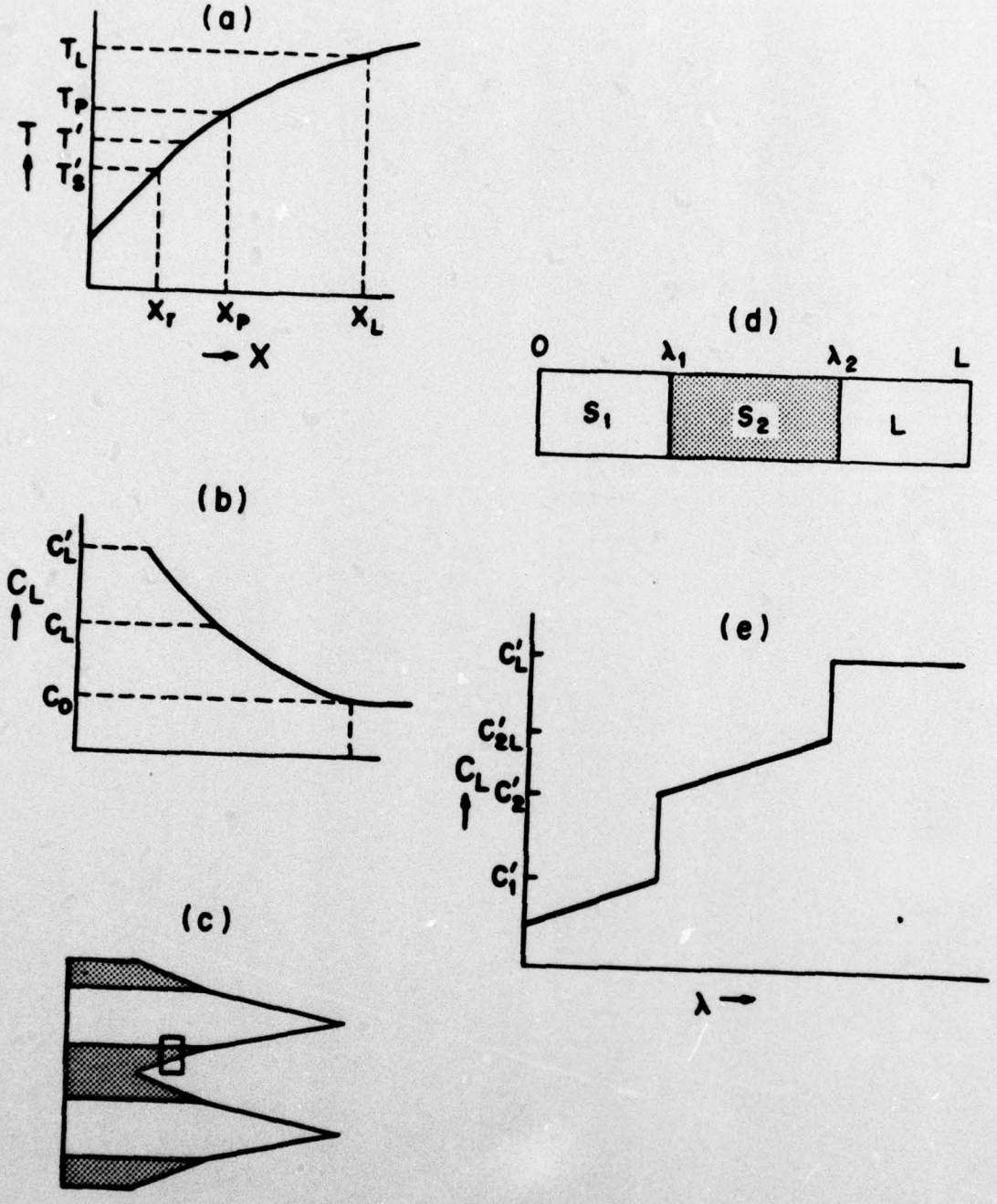

Figure 2. Model for directional solidification of peritectic alloys a). Temperature distribution during undirectional solidification b). Liquid composition in the solid and liquid and in the liquid region c). Illustration of the sequence of formation of solid phases indicating position of the characteristic volume element d). Sketch of a volume element considered in the solid and liquid region e). Concentration profile along the length of the volume element.

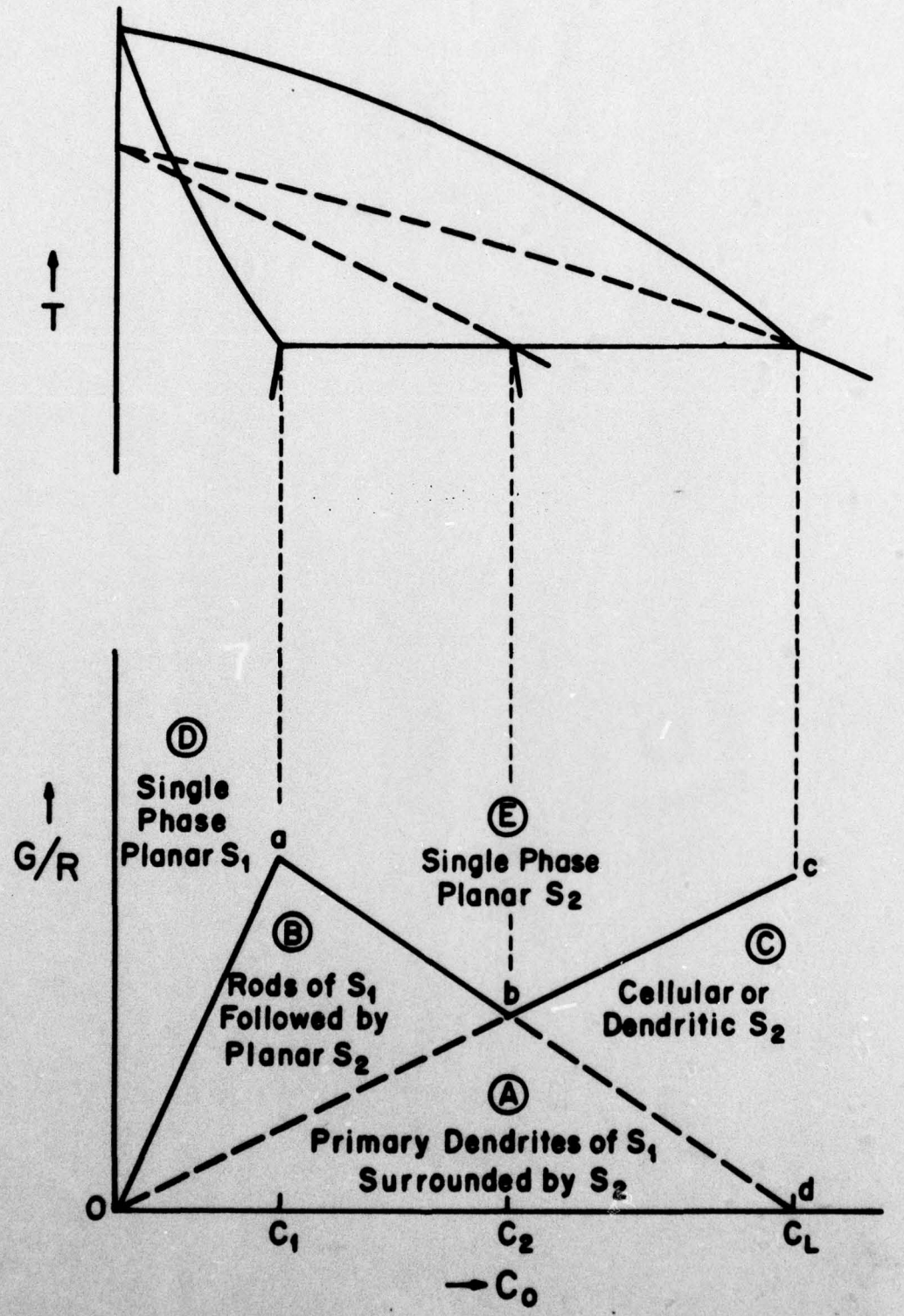

Figure 3. Critical G/R vs Co plot to obtain planar solid-liquid interface, as defined by equations 5-7. Also shown are the expected microstructures and interface morphology.

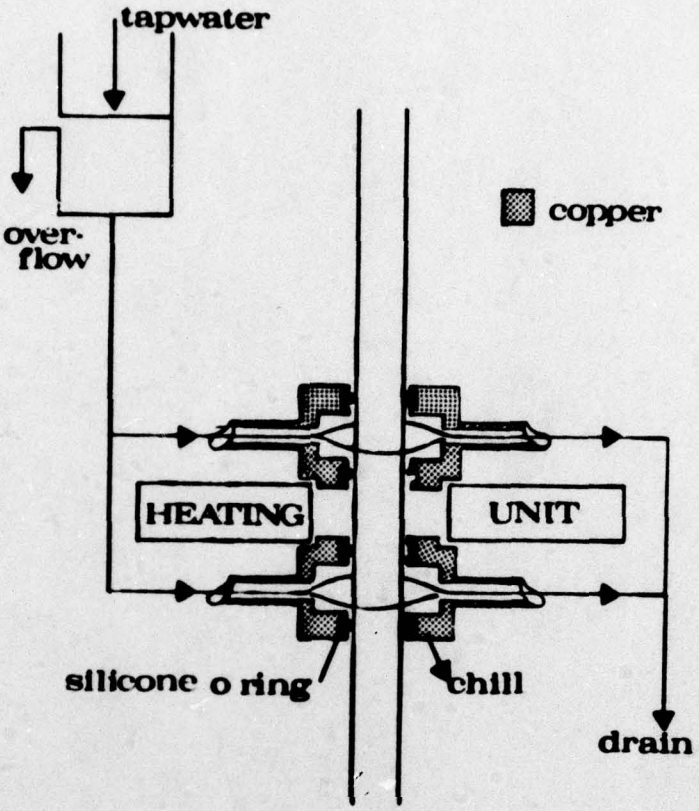

Figure 4. A low temperature vertical zone melting unit showing the heating and cooling arrangements.

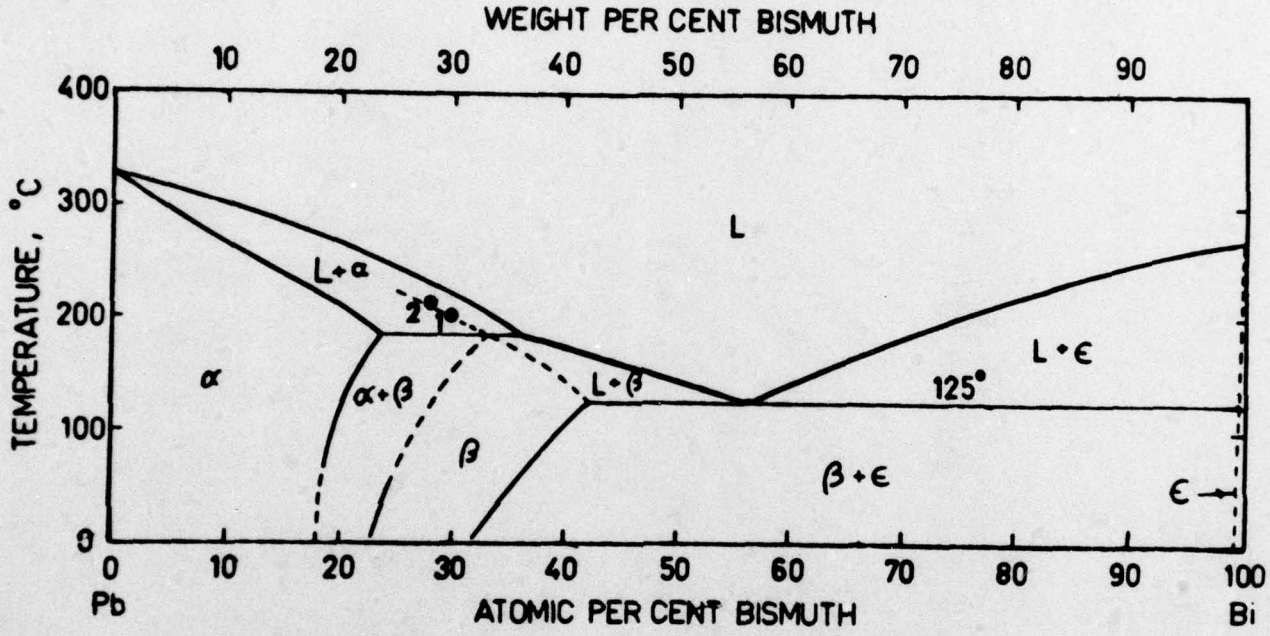

Figure 5. Constitution diagram of Pb-Bi system[16] with extended metastable solidus. Data points represent the actual interface temperatures measured at the solid (plane front β)/liquid interface.

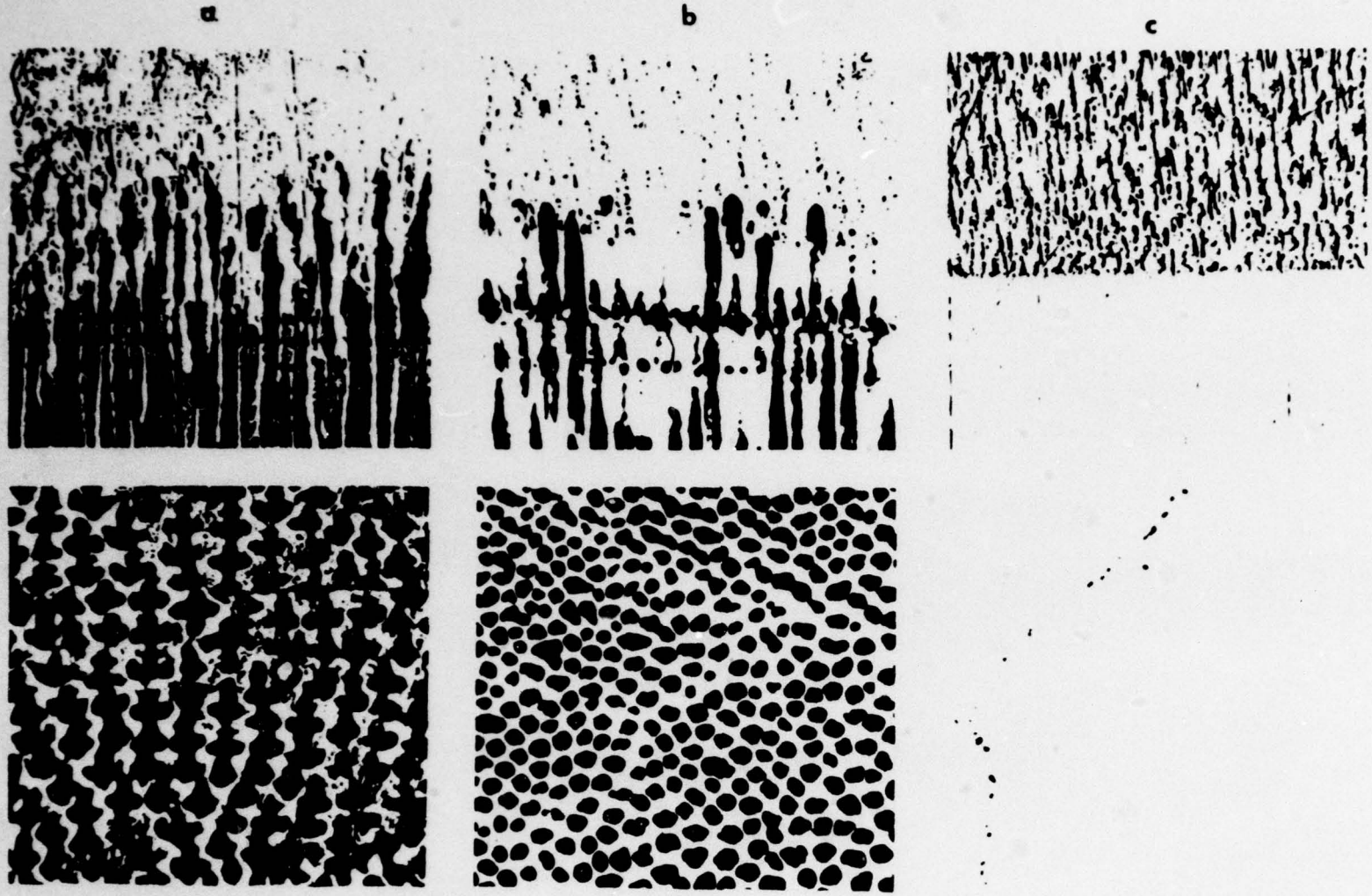

Figure 6. Typcial aligned structures showing the effect of G/R ratios. In each case the top photomicrograph is a logitudinal section including the quenched interface, and the bottom is a transverse section. (a) Co=28wt% Bi;G/R-1.03×10^{6}C-sec. per cm^2. (b) Co=28 wt% Bi; G/R-1.55×10^{6}C-sec per cm^2. (c) Co-28 wt% Bi; G/R-4.87×10^{6}C-sec per cm^2(50X).

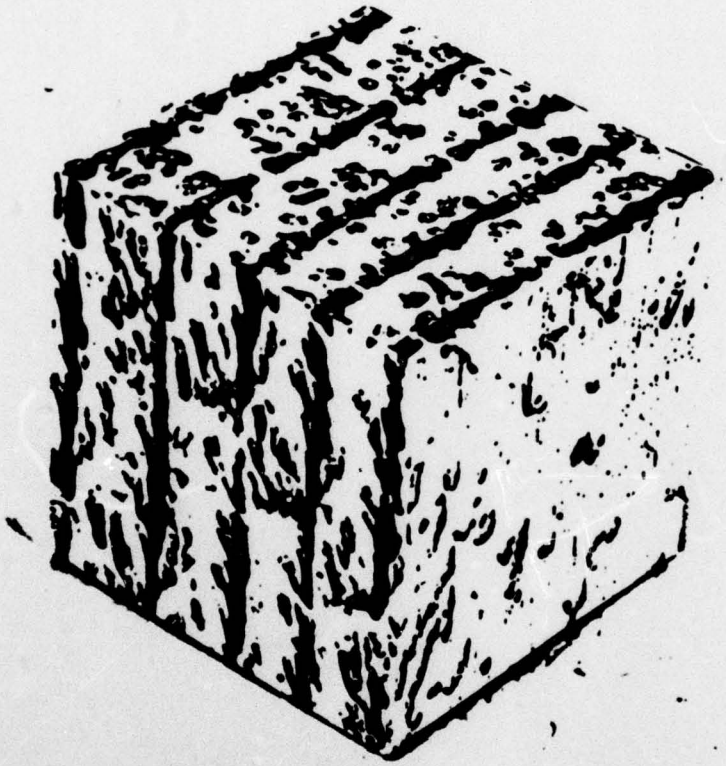

Figure 7. Three dimensional composite photomicrograph showing branched plate-like dendrites of α phase surrounded by β phase.

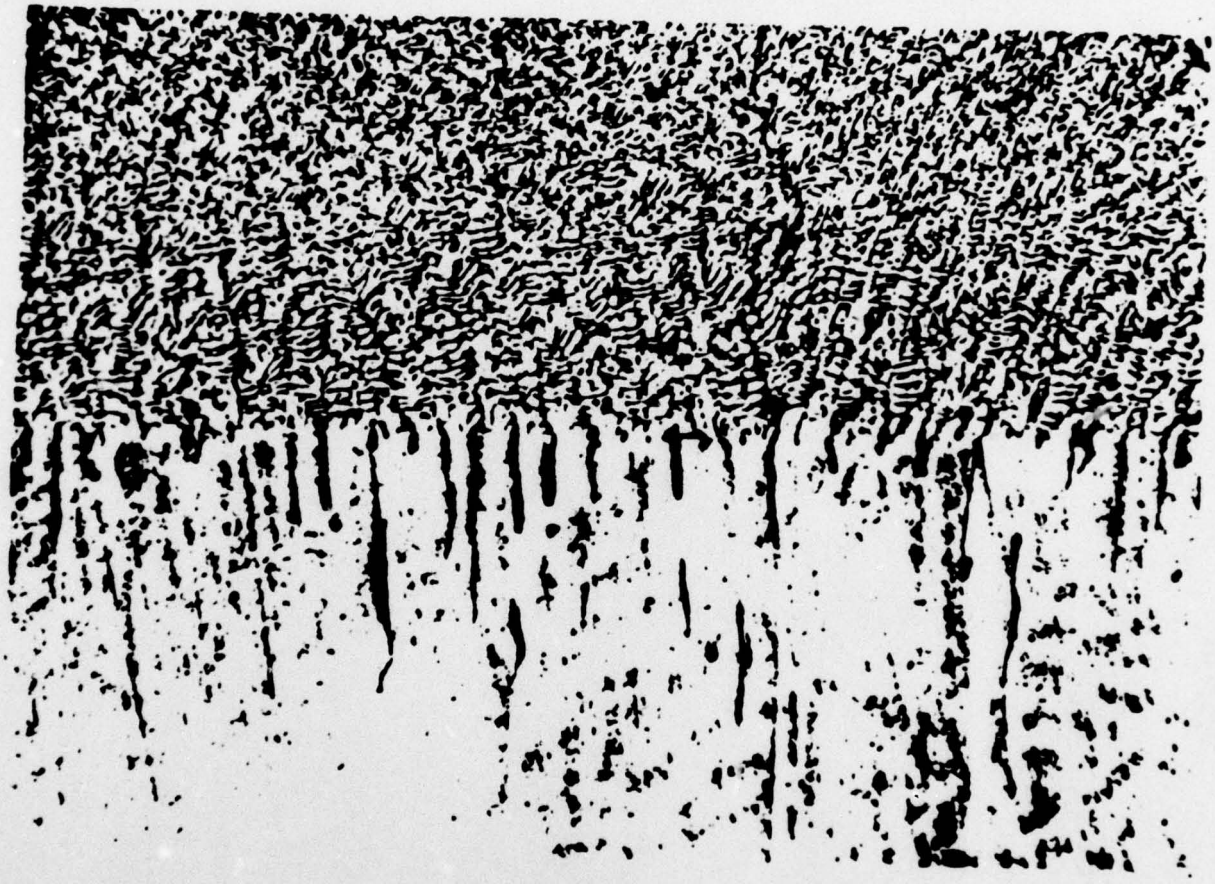

Figure 8. Photomicrograph of a quenched interface which is cellular β. (100X)

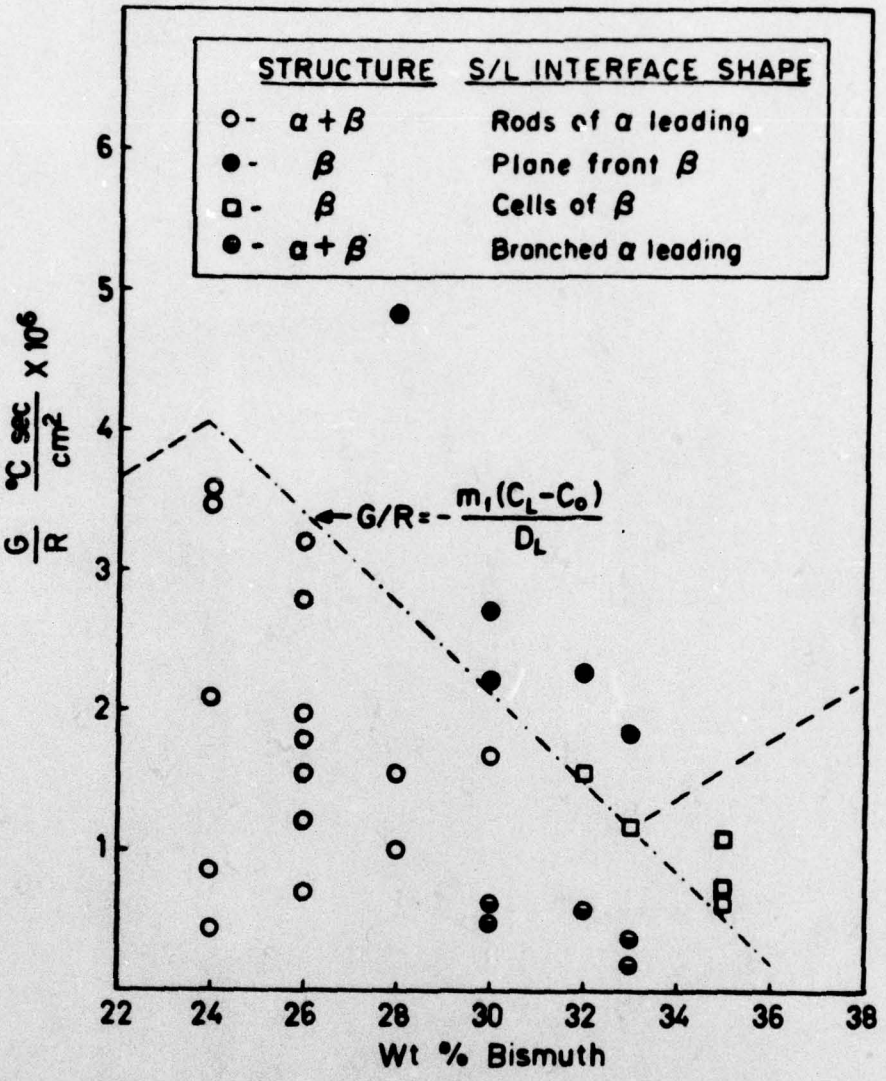

Figure 9. Structures of directionally solidified Pb-Bi alloys and interface shapes as a function of G/R and C_o.

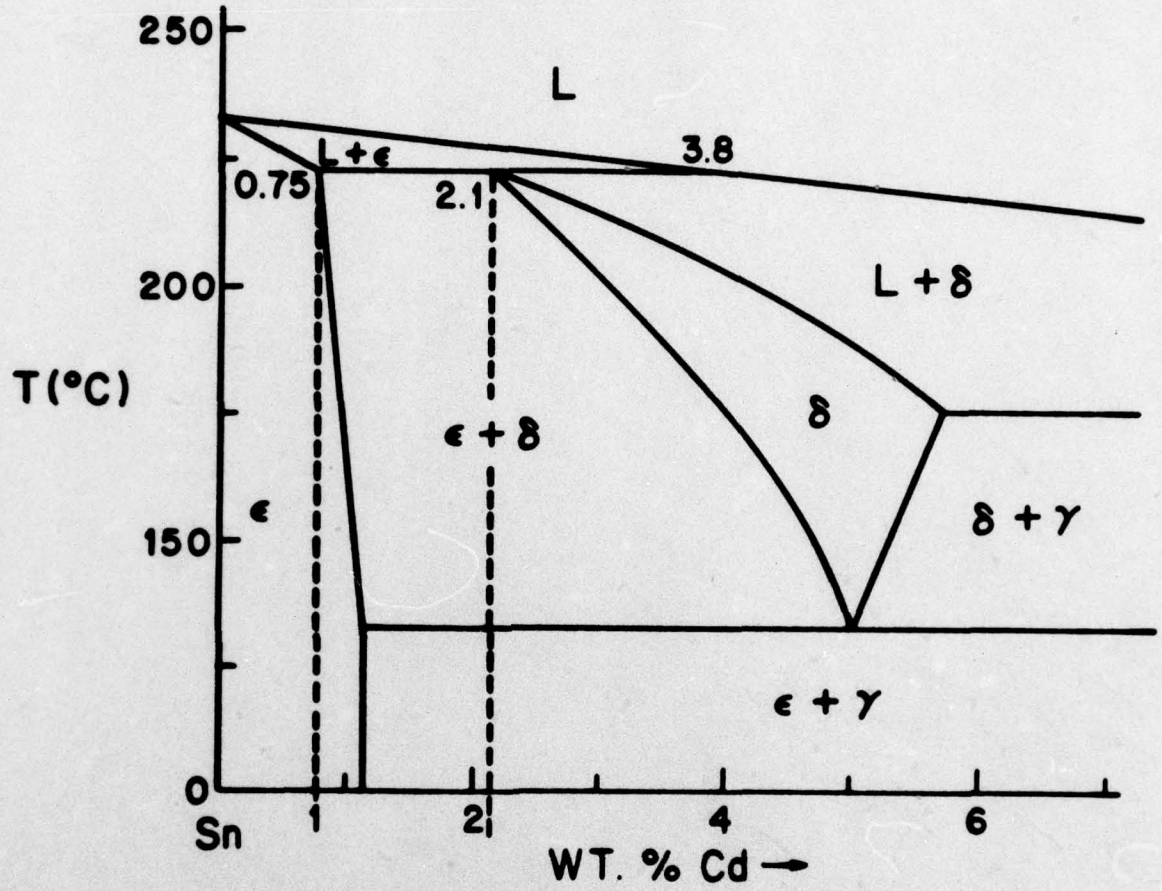

Figure 10. Constitution diagram of Sn-Cd system [17]

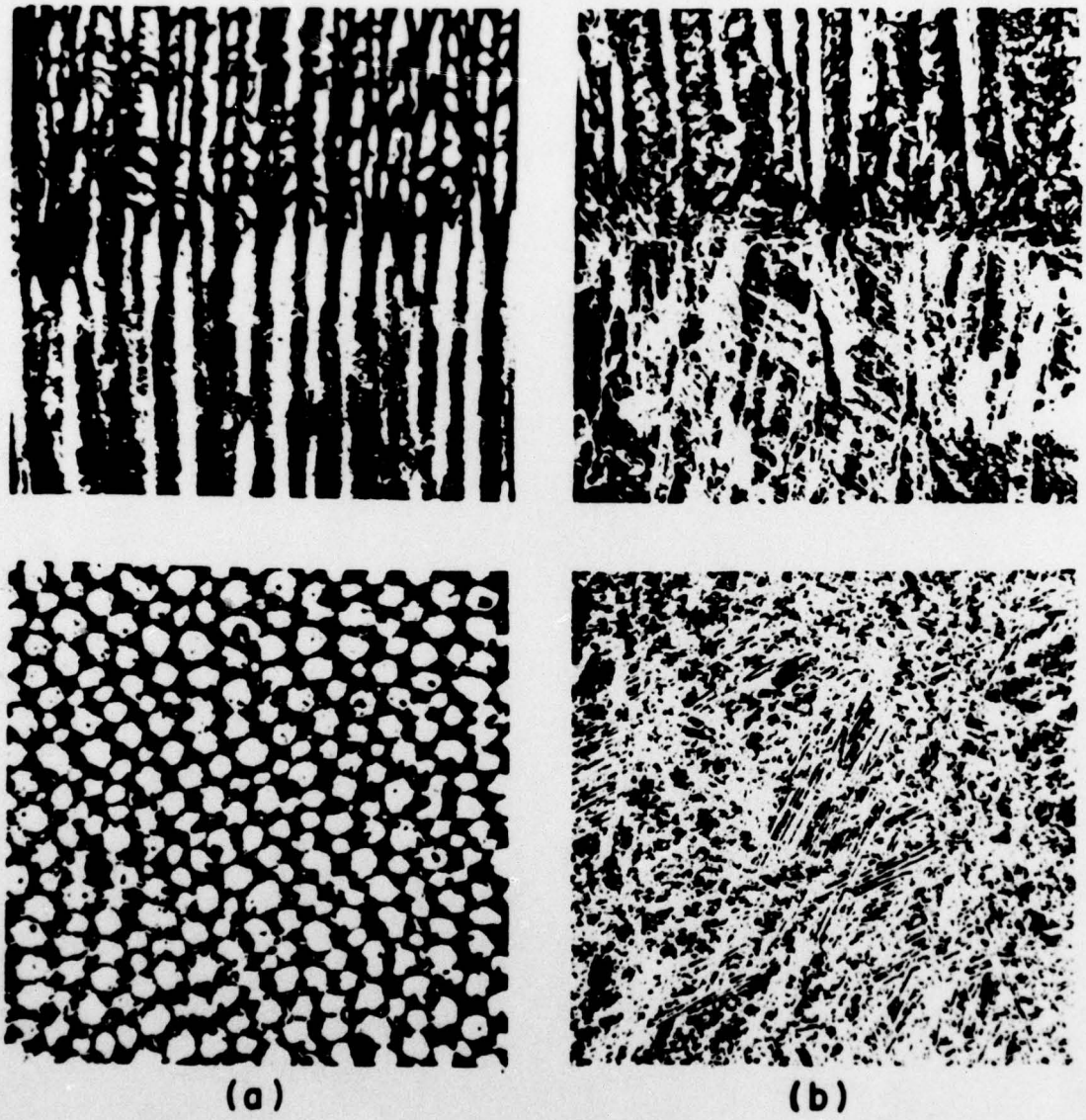

Figure 11. Typical longitudinal and transverse photomicrographs showing the effect of G/R ratios. (a) Co=1.5 wt% Cd; G/R=0.9×10^5 °C-sec per cm^2 (b) Co=1.5 wt% Cd; G/R=1.03×10^6 °C-sec per cm^2 (100X).

(a)

(b)

Figure 12. a) Photomicrograph of a longitudinal section including the quenched interface showing ϵ phase nucleating and growing along with δ phase without any interference with the planar solid-liquid interface.
b) Transverse photomicrograph of the same sample.

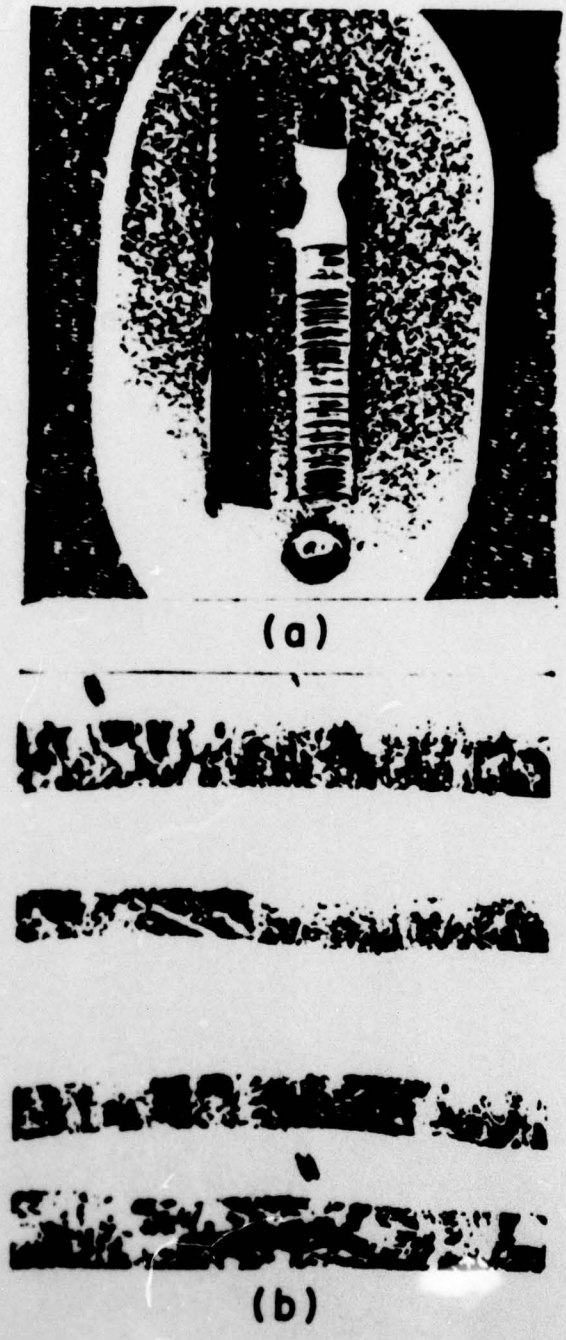

Figure 13. Banding in directionally solidified sn-cd alloys. a) Photomacrograph of directionally solidified sample (2X). b) Photomicrograph of the same sample showing alternate layers of ϵ and δ (50X)

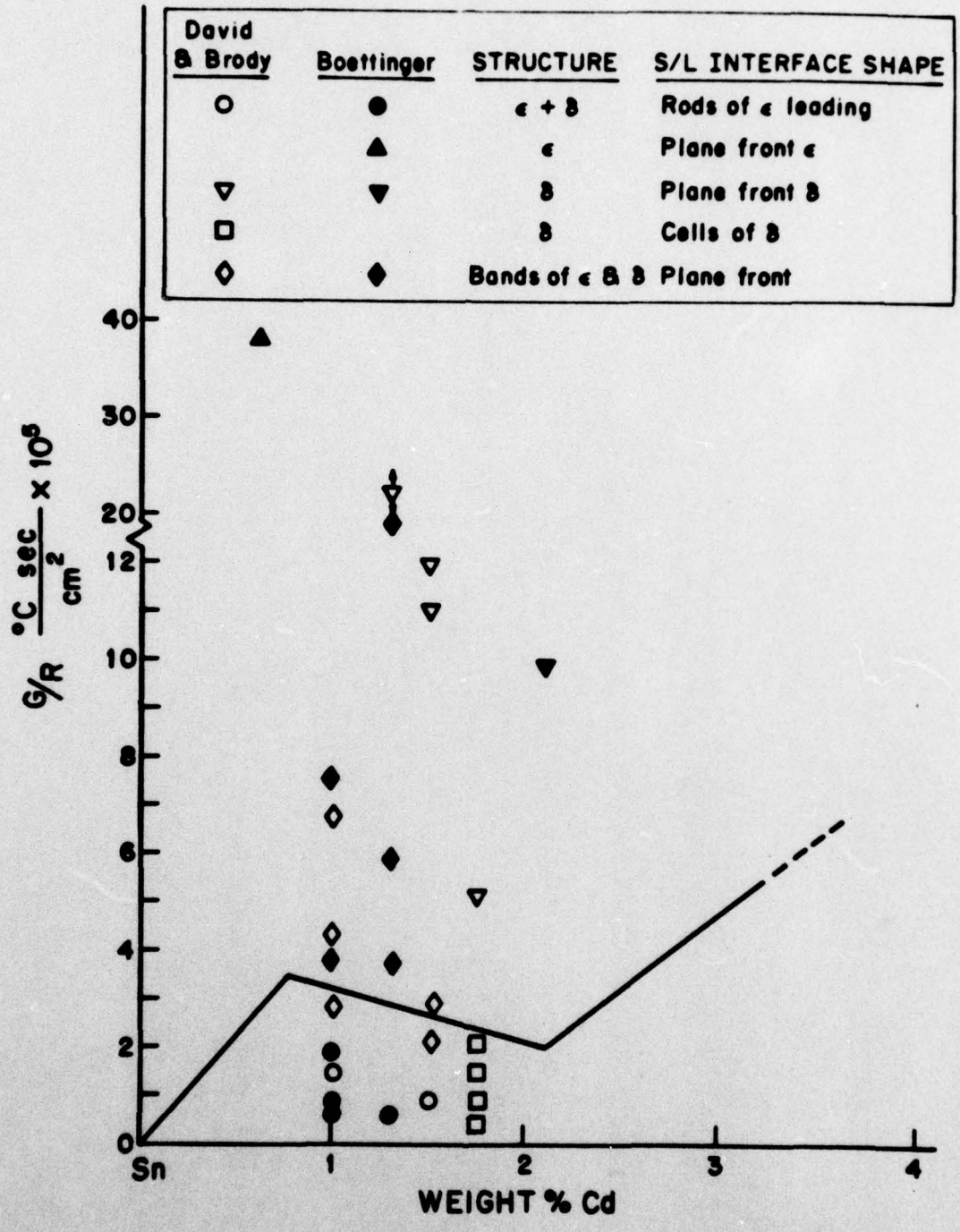

Figure 14. Structures of directionally solidified Sn-Cd alloys and interface shapes as a function of G/R and C_o.

SIMULATION OF HEAT FLOW AND THERMAL STRESSES IN AXISYMMETRIC CONTINUOUS CASTING

J. Mathew[+] and H. D. Brody*

Synopsis

Thermal stresses in continuous casting play a role in the development of casting defects such as hot tearing, cold cracking, and surface cracking. Hence, an ability to predict the level of thermal stresses in an ingot in relation to the casting conditions is important for the optimum design of continuous casting processes. The model described herein is a finite element analysis of heat flow and the development of thermal stresses in axisymmetric continuous casting applicable to the simulation of both ferrous and non-ferrous alloys. The model is capable of simulating a wide range of boundary conditions, and the program is simple to use. The model takes into account the heat flow and displacements in the axial and radial directions in the casting and accounts for the temperature dependence of material properties. The stress simulation employs a thermoelastic-plastic creep analysis and can compute both the elevated temperature stresses and the residual stresses in the ingot at room temperature.

The analysis is found to be useful in studying the formation of various thermal stress induced defects like hot tearing, surface cracking and cold cracking in continuously cast ingots. A parameter called maximum normalised stress (obtained by dividing the maximum (algebraic) stress by the yield stress of the material at the temperature of the region of interest) is found to correlate well with the observed relation between the hot tearing tendency

[+]Senior Research Engineer, Metallurgical Research Labs, Combustion Engineering, Inc., Chattanooga, Tennessee 37402, formerly Graduate Fellow, Univers ty of Pittsburgh.

*Professor and Chairman, Department of Metallurgical and Materials Engineering, University of Pittsburgh, Pittsburgh, Pennsylvania 15261.

of continuously cast aluminum and the casting rate. The analysis has been applied to predict the dependence of temperature profile and freezing (sump) profile in the casting on the casting rate. The predicted effect of the casting rate on the mold heat flux is found to be consistent with experimental measurements.

Analysis

Details of the analysis can be found in the references.[1,2,3] Only a brief description is given here. The heat flow simulation employs a finite element method to take into account the steady state heat transfer in the axial and radial directions in a cylindrical ingot. This makes the analysis applicable to the study of ferrous and non-ferrous metals like aluminum and copper which have fairly good conductivity and are cast at relatively slow speeds. This makes the axial heat transfer relatively important in continuous casting of these alloys. The axial heat transfer is not appreciable in continuous casting of steel except at the bottom of the mold where the radial resistance to heat transfer due to the air gap makes the axial heat transfer relatively important.

The model takes into account the variation of material properties with temperature and can handle both equilibrium or non-equilibrium solidification modes. (The results presented in this paper assume non-equilibrium solidification.) Hot tearing is believed[4-8] to originate in the mushy zone of the alloy near the effective solidus temperature. The fraction of liquid which is in equilibrium with the solid at any temperature within the mushy zone of the alloy and the effective solidus temperature of the alloy depend very much on whether equilibrium or non-equilibrium solidification is assumed.[9] The latent heat liberated during solidification can be incorporated into the specific heat or it may be incorporated into the enthalpy of the material.

The model has the flexibility to account for virtually all boundary conditions encountered in continuous casting. This includes, and is not limited to, a refractory header at the top of the mold (as customarily used in aluminum D.C. casting) and a delayed quench. In the mold region where an air gap generally forms, the position and extent of air gap formation can be computed by the analysis. Provision to compute the air gap formed is very important in the analysis of thermal stresses. The location and extent of air gap formation have a strong effect on the temperature field in the casting and hence on the thermal stresses, but have only a weak effect on the sump profile.[10]

The thermal stress analysis is also an axisymmetric finite element analysis. It takes into account the deformation in the axial as well as radial directions in the casting. (Previous analyses[11,12] of thermal stresses in continuous casting assumed a plane strain deformation. A plane strain assumption is not valid when there are thermal gradients in the withdrawal directions as in the continuous casting of aluminum.) The present analysis takes into account the elastic, plastic, creep and thermal deformations of the material. The analysis has flexibility to account for the variation of the material properties (stress-strain relations and creep law) with temperature. Virtually all boundary conditions encountered in continuous casting of cylindrical ingots can be accounted for in the analysis. This includes the effect of metallostatic head and mold friction forces. The analysis computes the stresses in the mushy zone of the alloy below the coherency temperature. The coherency temperature of an alloy is defined as the temperature above which the alloy behaves like a liquid and below which it behaves like a solid. It has been proposed[14] that the coherency temperature of an alloy plays a major role in deciding the hot tearing sensitivity of an alloy.

As the details of the validation of the model are given in references 1-3, only a brief description is given here for completeness. The heat transfer analysis was checked by comparing the model predicted temperature profiles and freezing profiles with measured quantities (both laboratory and industrial casting conditions for ferrous and non-ferrous continuous casting were checked). The agreement was found to be very good between the measured and calculated sump profiles and temperature fields. The stress analysis was checked by two methods. The displacement field was checked by comparing stress fields predicted by the model with analytical results for simple, ideal cases (not continuous casting) where analytical solutions are available. The agreement was found to be very good. Lastly, the application of the model to continuous casting was checked by applying the analysis to the D.C. casting of Al-Si alloy. The residual stresses in a D.C. cast ingot were measured by Roth, et al.[13] The residual stresses and positions of stress reversal predicted by the model were found to be in good agreement with those reported by Roth, et al. The results obtained from the analysis are the following:

(A) Temperatures and cooling rates at different positions in the casting.

(B) Position of the liquidus and solidus isotherms in the casting.

(C) Heat flux from the casting to the mold at different heights in the mold.

(D) Axial, radial, hoop, shear and equivalent stresses at different locations in the casting.

(E) Principal stresses and principal planes corresponding to stresses in (D).

(F) Maximum normalised stresses and hydrostatic stress at each location of the ingot and hydrostatic stress at different locations in the casting. Maximum normalised stress is obtained by dividing the maximum (algebraic) stress by the yield stress of the material at the temperature of the location where the stress is computed.

(G) Radial and axial deformations of the ingot.

(F) Plastic strains at different locations in the casting.

The analysis computes the elastic stresses in the absence of relaxation as well as the stresses after plastic flow and creep.

Application of the Model to an Al-Mg Alloy

Figure 1 shows the magnitudes and directions of the elastic thermal stresses in a 37 cm. diameter 5082 aluminum-magnesium alloy ingot cast at 5 cm./min. (As the casting conditions assumed in the simulation may not be encountered in actual practice, the example is given only for illustration.) The principal stresses are plotted to scale as vectors normal to the principal planes. The temperatures at positions where the stress is computed are indicated by numbers next to the stress vectors in Figure 1. To account for the coherency temperature of the alloy, the elements above the coherency temperature of the alloy have been removed from the assembly and proper boundary conditions due to metallostatic head have been applied. The stresses after plastic flow and creep have been taken into account and are shown in Figure 2. Notice that the magnitude and direction of the principal stresses have changed considerably after plastic flow and creep. The principal stresses are normal to the solidification front in the casting near the top of the ingot. This is to be expected as the metallostatic head acts normal to the solidification front. However, the principal planes rotate as the ingot is withdrawn and become aligned with the coordinate axes at lower temperatures. The existence of a neutral plane between the surface and the center of the casting also can be seen from the stress plots.

It is obvious from Figures 1 and 2 that the magnitude of the stresses change considerably at different locations in the casting. However, since the temperature also changes, the severity of the stresses cannot be obtained readily through the absolute stresses. In order to make the stress values more meaningful, the stress is normalised by dividing the computed stress values

by the yield stress of the material at the temperature considered. The maximum (algebraic) value of this quantity is selected and is called the maximum normalised stress.

Table 1 gives the maximum normalised stress at different positions in a 38 cm. diameter, 5082 Al-Mg alloy ingot poured at 8.9 cm./min. (3.5 in./min.). Negative signs before the stress values indicate compressive stresses. The axis of the ingot is at the right-hand column of the stress values). The maximum normalised tensile stress increases within the mushy zone and reaches a maximum near the solidus. The peak normalised stress near the solidification front can be related to the hot tearing tendency of D.C. cast aluminum alloys leading to "centerline" or "star" cracks.

Away from the solidification front, the maximum normalised stress decreases. However, near the bottom of the casting, it increases again and reaches another maximum. The peak in the maximum normalised stress at the bottom of the ingot may be related to the formation of cold cracks in non-ferrous alloys. Some as cast alloys (for example 7075 aluminum alloys) have very poor ductility at room temperature. Ingots of these alloys, if the residual stresses developed during the casting is high enough, will crack during cooling. These cracks, also, will be symmetric with respect to the axis of the ingot (since the peak of the maximum normalised stress occurs near the axis of the ingot). Since the cracks form after the ingot has been completely solidified, the cracks will be open (i.e., will not be healed by flow of liquid metal).

A third zone where a peak in the maximum normalised stress occurs is at the surface of the ingot. Referring to Table 1, a peak in the maximum normalised stress is found to occur near the mold exit. If these stresses exceed the strength of the material, surface cracks may form in the ingot.

Table 2 gives the maximum normalised stress in an ingot identical to that in Table 1 except that the ingot is cast at 10.2 cm./min. (4.0 in./min.). The effect of increasing the casting rate on the maximum normalised stress

can be studied by comparing Tables 1 and 2. Notice that the maximum normalised stress near the solidification front of the ingot increases from 1.7 to 3.5 as the casting rate is increased from 8.9 cm./min. to 10.2 cm./min. Thus, according to the model, the hot tearing (star cracking) tendency of the ingot should increase with increase in casting rate. This is confirmed from industrial experience.[1,15-18] From results of experiments available to us, the ingot simulated in Tables 1 and 2 can be cast without cracking at 8.9 cm./min., whereas it would exhibit fine centerline cracks when cast at 10.2 cm./min.

From Tables 1 and 2 it is also seen that the maximum normalised stress near the surface of the ingot increases with decrease in the casting rate. This is to be expected, as the air gap formed will be smaller and the resultant reheating of the ingot will be less for lower casting rates. It is also of interest to note that the residual stresses (at the end of cooling of the ingot) decrease with increase in casting rate. The residual stresses are useful in studying the tendency of the ingot to cold cracking. However, it should be pointed out that coldcracking is influenced both by the stresses and plastic strains. The present simulation gives both the stresses and the plastic strains for use in studying the cold cracking of continuously cast ingots.

Effect of Casting Rate on the Temperature Profile

Figure 3 shows the effect of casting rate on the surface and center temperature profiles in a 5082 Al-Mg alloy ingot. The casting rate is found to have a considerable effect on the center temperature profile. However, the surface temperature profile is practically insensitive to casting rate. (These observations are in agreement with measurements of thermal profile in continuous casting using thermocouples, etc.[15,18]) Since increasing the casting

rate is found to increase the hot tearing tendency of a casting, one way to explain the hot tearing tendency of the casting is to explain it with reference to the differences in surface and center cooling rates. Bryson[15] has done this for A6063 alloy. He defined a "hot cracking parameter," the difference in cooling rates between the center and the surface of the casting, which he used successfully in explaining the hot tearing sensitivity. Table 3 gives the center and surface cooling rates between the center and the surface of the casting, which he used successfully in explaining the hot tearing sensitivity. Table 3 gives the center and surface cooling rates in 16 cm. and 38 cm. diameter ingots cast at different speeds. The hot cracking parameter is indeed found to increase with increase in casting rate. However, as can be seen from Table 3, this parameter fails to explain the size effect on hot tearing sensitivity.

Effect of Casting Rate on the Freezing Profile

The freezing profile in a casting is very important as this has a predominant effect on the formation of defects. For example, a long sump in a casting may give problems with fluid flow induced defects such as segregation, etc.[19,20] The sump depth also has a great effect on the feeding of the casting. For example, a bowed sump[21] may result in the formation of porosity and associated defects.

Figure 4 shows the effect of casting rate on the position of the solidus and liquidus isotherms in a 38 cm. diameter casting. Increasing the casting rate is found to increase the sump depth considerably. The strong influence of casting rate on the sump depth has been observed by many investigators[10,19,22-34] who by means of techniques such as the breakout method, adding radioactive tracers and pellets, inserting metal rods into the sump, etc., have measured the sump depth in continuous casting. However, the striking feature of Figure 4 is that with increase in casting speed the separation between

the solidus and liquidus isotherms increases. This increases the size of the mushy zone in the casting. One of the main reasons for the increased tendency of the casting to hot tear at high casting speeds is probably its effect on the cooling rates existing in the casting and on the freezing profile in the casting.

Heat Flux from the Surface of the Ingot

Table 4 gives the influence of casting rate on the heat flux from the surface of a 38 cm. diameter casting. The heat flux is found to increase with the increase in casting speed. This is consistent with the observations of Singh and Blazek[35] who measured the heat flux in the mold of a continuous caster at different casting speeds.

Summary

The analysis presented here is useful in studying the formation of various thermal stress induced defects such as hot tears, surface cracks and cold cracks in continuously cast ingots. The analysis is found to predict correctly the effect of casting rate on the hot tearing tendency of the casting. Thus, the analysis can be 'calibrated' through experiments to determine the maximum casting rate at which an ingot may be cast without cracking. Once this information is available for typical conditions, the analysis may be used to optimize casting conditions taking into account stress induced defects. Thus, the present simulation provides a powerful tool to the operators of continuous casting installations.

Acknowledgements

The authors are grateful to the Office of Naval Research (Contract N0014-67-A-0402-0003) and the ALCOA Foundation for contributing to the support of this project. The computations were performed at the Computer Center, University of Pittsburgh on the DEC-10 system.

References

1. J. Mathew, Ph.D. Dissertation, Department of Metallurgical and Materials Engineering, University of Pittsburgh, Pittsburgh, Pa. 15261, 1977.
2. J. Mathew and H. D. Brody, "Analysis of Heat Transfer in Continuous Casting Using a Finite Element Method," Computer Simulation for Materials Applications, Nuclear Metallurgy, R. J. Arsenault, et al. (eds.), Vol. 20, Part 2 (1976), pp. 1138-1150.
3. J. Mathew and H. D. Brody, "Simulation of Thermal Stresses in Continuous Casting Using a Finite Element Method," Computer Simulation for Materials Applications," Nuclear Metallurgy, R. J. Arsenault, et al. (eds.), Vol. 20, Part 2 (1976), pp. 978-990.
4. T. Morinaga, et al., "Fundamental Investigation of Hot Tearing in Light Metals," Proceedings of the 31st International Foundry Congress, (Amsterdam, Paper No. 11.
5. J. Van Eeghem and deSy, "A Contribution to Understanding the Mechanism of Hot Tearing of Cast Steel," AFS Trans., Vol. 73 (1965), pp. 282-291.
6. J. A. Williams and A. R. E. Singer, "Deformation, Strength and Fracture the Solidus Temperature," Journal of the Institute of Metals, Vol. 96 (1968), pp. 5-12.
7. S. A. Metz and M. C. Flemings, "Hot Tearing in Cast Metals," AFS Trans., Vol. 77 (1969), pp. 329-334.
8. S. A. Metz and M. C. Flemings, "A Fundamental Study of Hot Tearing," AFS Trans., Vol. 78 (1973), pp. 453-460.
9. T. F. Bower, H. D. Brody and M. C. Flemings, "Measurements of Solute Redistribution in Dendritic Solidification," Trans. of TMS-AIME, Vol. 236 (1966), pp. 624-634.

10. J. K. Brimacombe and F. Weinberg, "Continuous Casting of Steel-Part 2: Theoretical and Measured Liquid Pool Profiles in the Mold Region During the Continuous Casting of Steel," Journal of the Iron and Steel Institute, Vol. 211 (January, 1973), pp. 24-33.

11. J. Moriceau,"Thermal Stresses in Continuous D.C. Casting of Aluminum Alloys: Discussion of Hot Tearing Mechanisms," Light Metals, 1975, (New York: The Metallurgical Society of AIME, 1975), pp. 119-134.

12. A. Grill, J. K. Brimacombe, and F. Weinberg, "Mathematical Analysis of Stresses in Continuous Casting of Steel," Ironmaking and Steelmaking, No. 1 (1976), pp. 38-47.

13. A. Roth, et al., Aluminum, Vol. 24 (1942), p. 206.

14. R. J. Claxton, "Aluminum Alloy Coherency," Continuous Casting, K. R. Olen, ed. (New York: TMS-AIME, 1973), pp. 341-352.

15. N. B. Bryson, "Increasing the Productivity of Aluminum D.C. Casting," Light Metals 1972, (New York: The Metallurgical Society of AIME, 1972), pp. 429-431.

16. Nomenclature of Continuous Casting Defects Group of the Steelmaking Division, British Iron and Steel Research Association, Definitions and Causes of Continuous Casting Defects (London: The Iron and Steel Institute, 1967).

17. A. G. Shakespeare, "Surface and Internal Defects," Continuous Casting of Ferrous and Non-Ferrous Metals (National Trade Press, 1966), pp. F1-F8.

18. D. G. Harrington, Kaiser Aluminum, Mt. Pleasant, California, private communication.

19. D. M. Lewis and J. Savage, "The Principles of Continuous Casting of Metals, Metallurgical Reviews, Vol. 1, Part 1 (1956), pp. 65-118.

20. W. M. Wojcik, "Segregation During Solidification of Small Continuously Cast Billets," Continuous Casting, K. R. Olen, ed. (New York: TMS-AIME, 1973), pp. 217-236.

21. D. D. Beattie, et al., "Control of Peripheral Zone Structure in Direct Chill Cast Aluminum," Proceedings of Conference on Modelling and Simulation for Applied Control Systems, (University of Bath: Institute of Measurement and Control, 1973), pp. 57-65.

22. D. A. Peel and A. E. Pengelly, "Heat Transfer, Solidification and Metallurgical Structure in the Continuous Casting of Aluminum," Mathematical Models in Metallurgical Process Development (London: Iron & Steel Institute, Publication 123).

23. D. A. Peel, A. E. Pengelly and S. Pilkington, "Pilot Plant Studies of Heat Transfer, Solidification and Resultant Structure of Continuously Cast Aluminum," Proceedings of the AIME Annual Meeting, Denver 1970.

24. E. A. Mizikar, "Mathematical Heat Transfer Model for Solidification of Continuously Cast Steel Slabs," Transactions TMS-AIME, Vol. 39 (November, 1967), pp. 1747-1753.

25. J. W. Donaldson and M. Hess, "Computer Simulation of Heat Transfer in Continuous Billet Casting," Continuous Processing and Process Control, T. R. Ingraham, ed. (New York: Gordon and Breach Science Publishers, 1968), pp. 299-320.

26. D. J. O. Adenis, K. H. Coats and D. V. Ragone, "An Analysis of the Direct-Chill Casting Process by Numerical Methods," Journal of the Institute of Metals, Vol. 91 (1962-63), pp. 395-403.

27. A. D. Akimenko, et al., Continuous Casting of Steel (London: The Iron and Steel Institute, 1962), p. 59.

28. J. J. Gautier, Y. Morillon and J. Dumont-Fellow, "Mathematical Study of the Continuous Casting of Steel," Journal of the Iron and Steel Institute, Vol. 208 (December, 1970) pp. 1053-1059.

29. R. D. Pehlke, ASM Metals Engr Quarterly, Vol. 4, No. 2 (May, 1964), p. 42.

30. R. D. Pehlke, "Unidirectional Analysis of Heat Transfer During Continuous Casting," Computer Applications in Metallurgical Engineering, R. D. Pehlke and M. J. Sinnott, ed. (Metals Park, Ohio: ASM, 1964), pp. 75-81.

31. L. Saroff, "Two Dimensional Heat Transfer Simulation of Continuous Casting-Its Uses in Design and Operation," Continuous Casting, K. R. Olen, ed. (New York: TMS-AIME, 1973), pp. 323-340.

32. J. Lait, et al., "A Comparison of Calculated and Observed Liquid Pool Profiles and Pool Depths in the Continuous Casting of Steel," Continuous Casting, K. R. Olen, ed. (New York: TMS-AIME, 1973), pp. 171-196.

33. J. Szekely and R. T. Yadoya, "The Physical and Mathematical Modelling of the Fluid Flow Field in the Mold Region in Continuous Casting Systems; Part 1-Model Studies with Aqueous Systems," Metallurgical Transactions, Vol. 3 (October, 1972), pp. 2673-2680.

34. S. K. Morton and F. Weinberg, "Continuous Casting of Steel-Part I: Pool Profile, Liquid Mixing and Cast Structure in the Continuous Casting of Mild Steel," Journal of the Iron and Steel Institute, Vol. 211 (January, 1973), pp. 13-23.

35. S. N. Singh and K. E. Blazek, "Heat Transfer Profiles in Continuous Casting Mold as a Function of Various Casting Parameters," Proceedings of AIME NOH BOSC Meeting, St. Louis, March 28-31, 1976.

Table 1

Maximum Normalised Stress in a 38 cm Diameter 5082 Al-Mg Alloy Ingot Cast at 8.9 cm/min (3.5 in/min) (Axial and radial divisions are equally spaced. Axial divisions are 2.5 cm)

Maximum normalized stress

1	3.075						
2	5.333	-0.698					
3	2.913	-0.207					
4	1.185	0.489	-0.285				
5	0.666	0.608	-0.086				
6	0.567	0.751	-0.305	-0.411			
7	0.519	0.794	-0.925	-0.696			
8	0.461	0.798	-0.595	-1.578	-1.376		
9	0.393	0.816	0.421	-2.795	-2.255		
10	0.312	0.817	0.966	-2.154	-4.214	-8.348	
11	0.214	0.816	1.057	-0.708	-6.178	-7.375	
12	0.149	0.750	0.933	0.401	-3.709	-9.200	
13	0.120	0.688	0.811	1.119	-1.258	-6.839	
14	0.113	0.691	0.829	1.476	0.517	-2.984	
15	0.112	0.698	0.838	1.354	1.681	-0.263	
16	0.113	0.680	0.871	1.237	1.716	1.517	Axis of ingot
17	0.113	0.651	0.908	1.164	1.451	1.495	
18	0.110	0.611	0.946	1.133	1.330	1.273	
19	0.104	0.566	0.961	1.179	1.282	1.160	
20	0.092	0.521	0.966	1.265	1.323	1.174	
21	0.078	0.483	0.972	1.344	1.472	1.319	
22	0.081	0.456	0.991	1.439	1.640	1.552	
23	0.081	0.450	1.035	1.542	1.828	1.813	
24	0.070	0.458	1.108	1.673	2.035	2.095	
25	0.074	0.476	1.201	1.829	2.259	2.385	
26	0.090	0.503	1.302	2.001	2.494	2.674	
27	0.111	0.524	1.387	2.164	2.725	2.957	
28	-0.042	0.433	1.438	2.288	2.887	3.216	

Bottom of ingot

Table 2

Maximum Normalised Stress in a 38 cm Diameter 5082 Al-Mg Alloy Ingot Cast at 10.2 cm/min (4.0 in/min) (Axial and radial divisions are equally spaced. Axial divisions are 2.5 cm)

Maximum normalized stress

1	1.801						
2	3.512	-0.233					
3	2.240	-0.103					
4	0.974	0.446	-0.434				
5	0.641	0.146	0.515				
6	0.534	0.468	-0.456				
7	0.464	0.814	-0.979	-0.647			
8	0.403	1.004	-1.294	-0.871			
9	0.340	1.001	0.062	-1.909	-1.610		
10	0.274	0.969	0.954	-3.137	-2.606		
11	0.208	0.906	1.304	-1.991	-4.635	-9.370	
12	0.131	0.859	1.101	-0.414	-6.553	-7.820	
13	0.089	0.767	1.050	0.731	-4.404	-9.265	
14	0.078	0.659	1.030	1.480	-1.637	-8.439	
15	0.080	0.676	0.990	2.389	0.729	-4.510	
16	0.089	0.690	0.970	2.341	2.229	-0.517	
17	0.097	0.688	0.985	1.870	3.465	2.122	
18	0.101	1.668	1.012	1.655	2.661	3.304	Axis of ingot
19	0.098	0.631	1.056	1.541	2.138	1.186	
20	0.087	0.581	1.084	1.513	1.947	1.876	
21	0.072	0.529	1.092	1.562	1.896	1.802	
22	0.073	0.486	1.097	1.625	1.975	1.893	
23	0.070	0.466	1.114	1.684	2.118	2.081	
24	0.056	0.462	1.152	1.757	2.258	2.320	
25	0.055	0.469	1.209	1.848	2.402	2.558	
26	0.070	0.485	1.275	1.952	2.546	2.779	
27	0.101	0.514	1.335	2.049	2.684	2.976	
28	-0.041	0.546	1.417	2.121	2.767	3.146	

Bottom of ingot

TABLE 3

Effect of Casting Rate on
Cooling Rates at the Time the Center
of the Casting Solidifies

Casting Rate cm./min.	Surface Cooling Rate °C/sec.	Center Cooling Rate °C/sec.	Difference Between Center and Surface Cooling Rates
		16 cm Diameter Casting	
10.0	1.84	8.23	6.39
17.5	2.14	13.40	11.26
25.0	2.20	14.40	12.20
30.5	1.91	18.22	16.31
37.5	2.03	19.79	17.76
		38 cm Diameter Casting	
5.0	0.17	1.96	1.80
7.5	0.10	2.90	2.80
8.9	0.18	3.14	2.96
10.0	0.14	3.46	3.32
12.5	0.17	3.73	3.56

TABLE 4

Effect of Casting Rate on the Heat Flux (cgs)
in a 38 cm Diameter Casting

Distance from the Meniscus, cm	Casting Rate (cm/min) 5.0	7.6	8.9	12.7
1.25	22.33	29.38	31.54	85.06
3.75	2.39	2.48	2.64	2.90
6.25	56.92	63.85	67.59	75.48
8.75	28.39	34.07	36.29	43.35
11.25	21.19	26.32	22.85	33.93
13.75	16.76	21.47	19.39	28.25
16.25	13.71	18.14	16.90	24.38

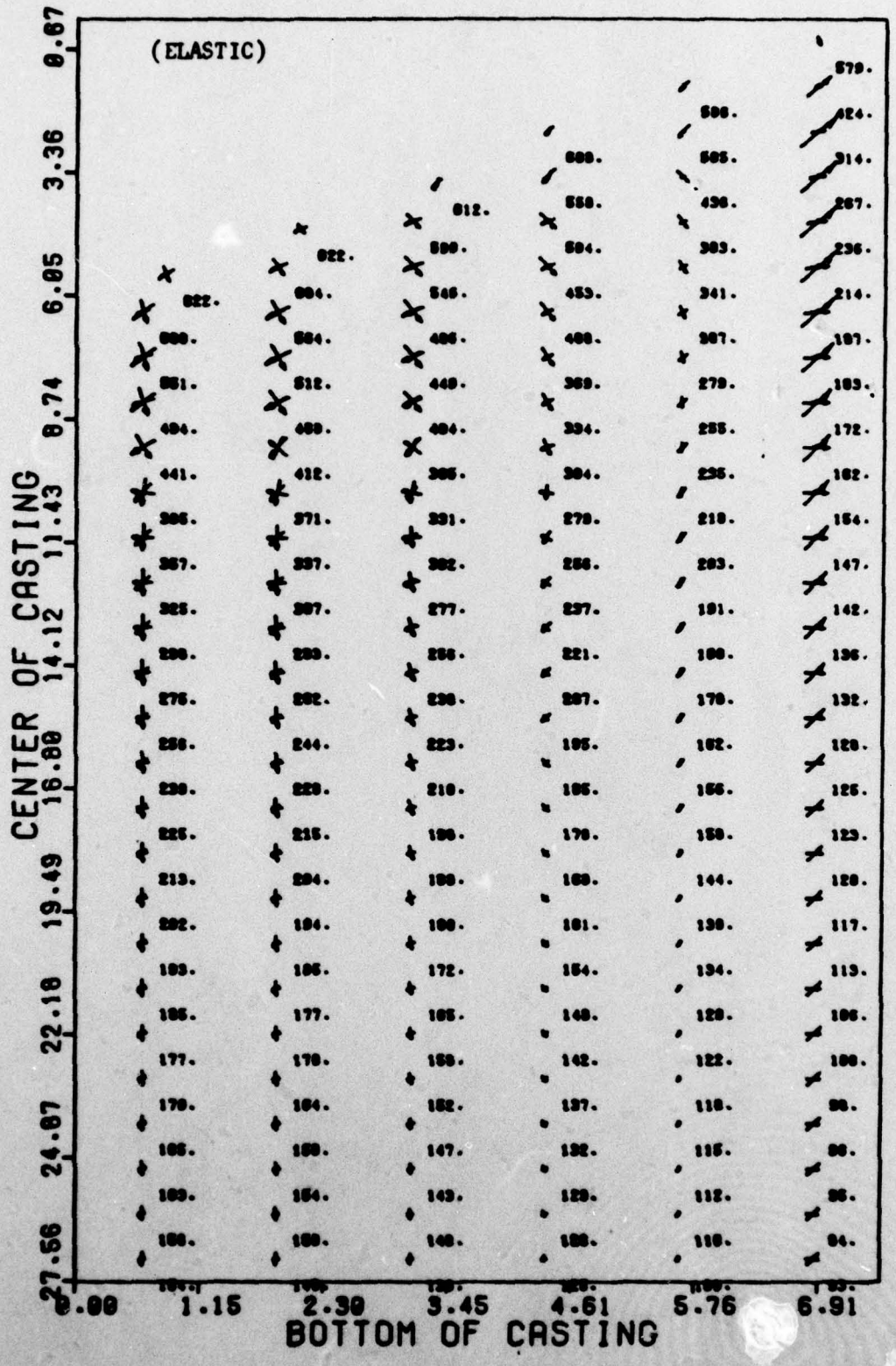

Figure 1 Elastic stress distribution in a 38 cm diameter ingot cast at 5 cm/min. Numbers indicate temperature. Arrows indicate principal stress magnitudes and directions. One centimeter is equivalent to 31 kg/mm^2 (44,000 psi).

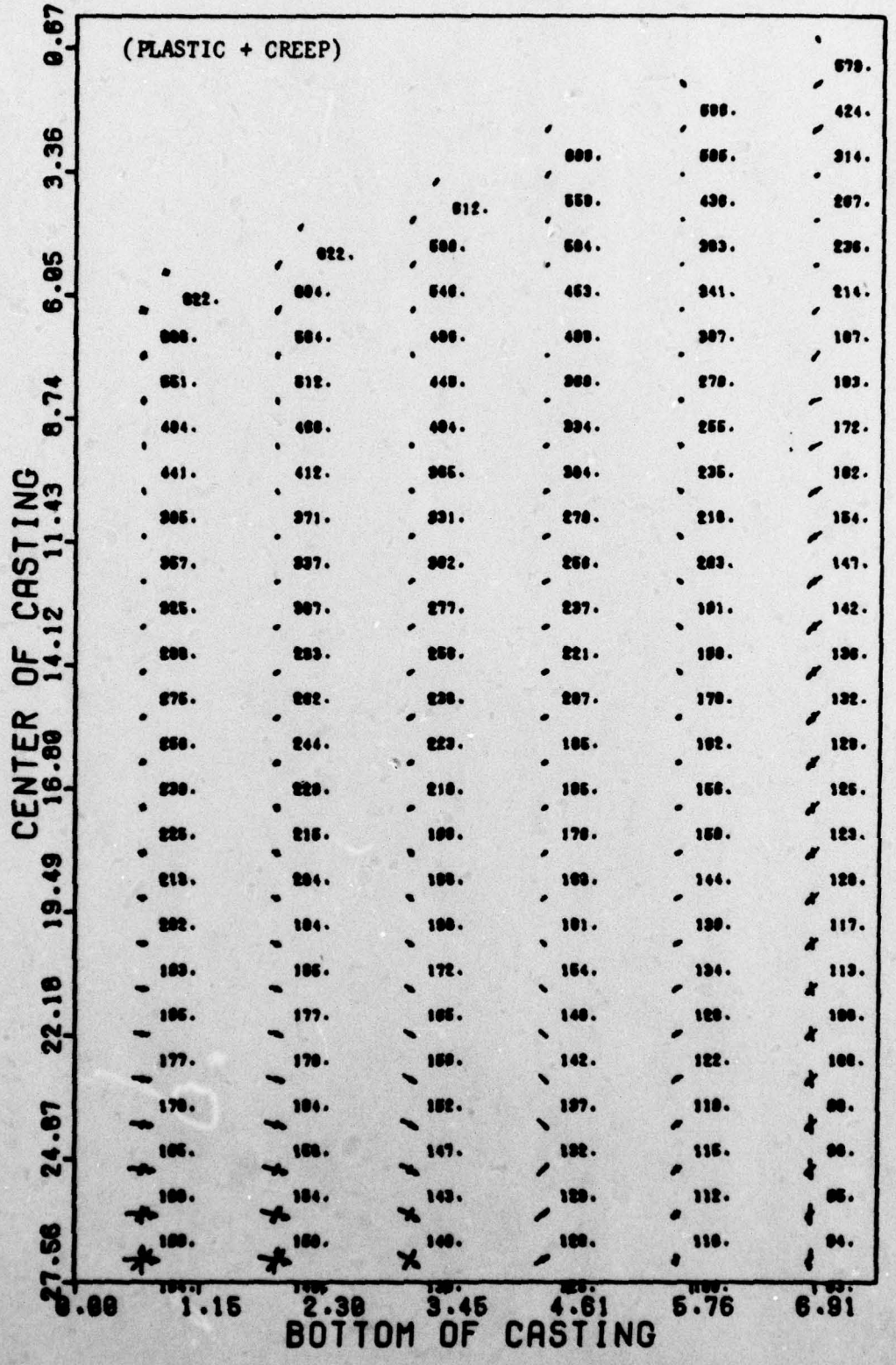

Figure 2 Stress distribution after plastic flow and creep in a 38 cm diameter ingot cast at 5 cm/min. Numbers indicate temperature. Arrows indicate principal stress magnitudes and directions. One centimeter is equivalent to 50 kg/mm^2 (70,000 psi).

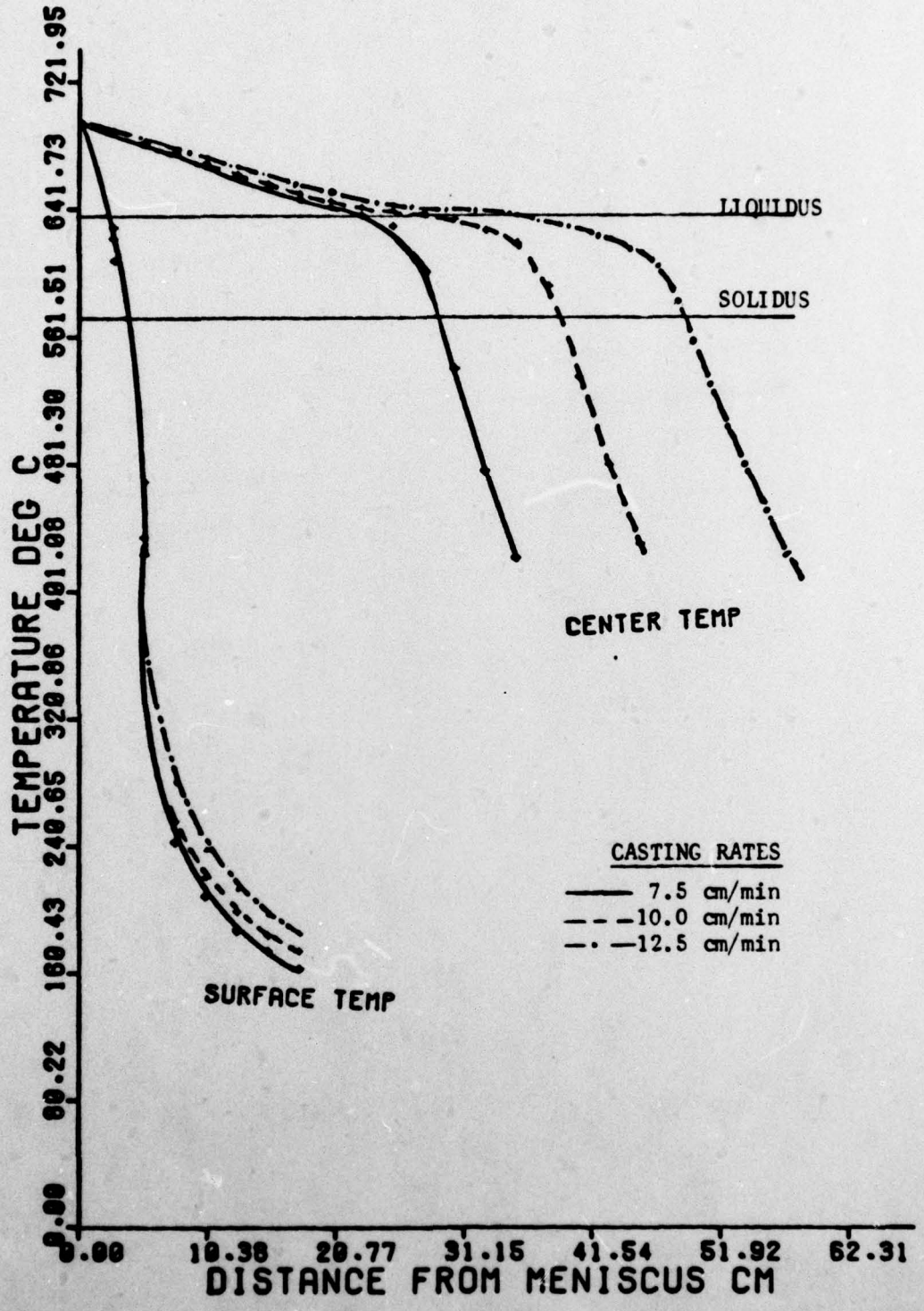

Figure 3 Effect of casting rate on the temperature profile in 5082 Al-Mg alloy ingot cast at 7.5, 10 and 12.5 cm/min.

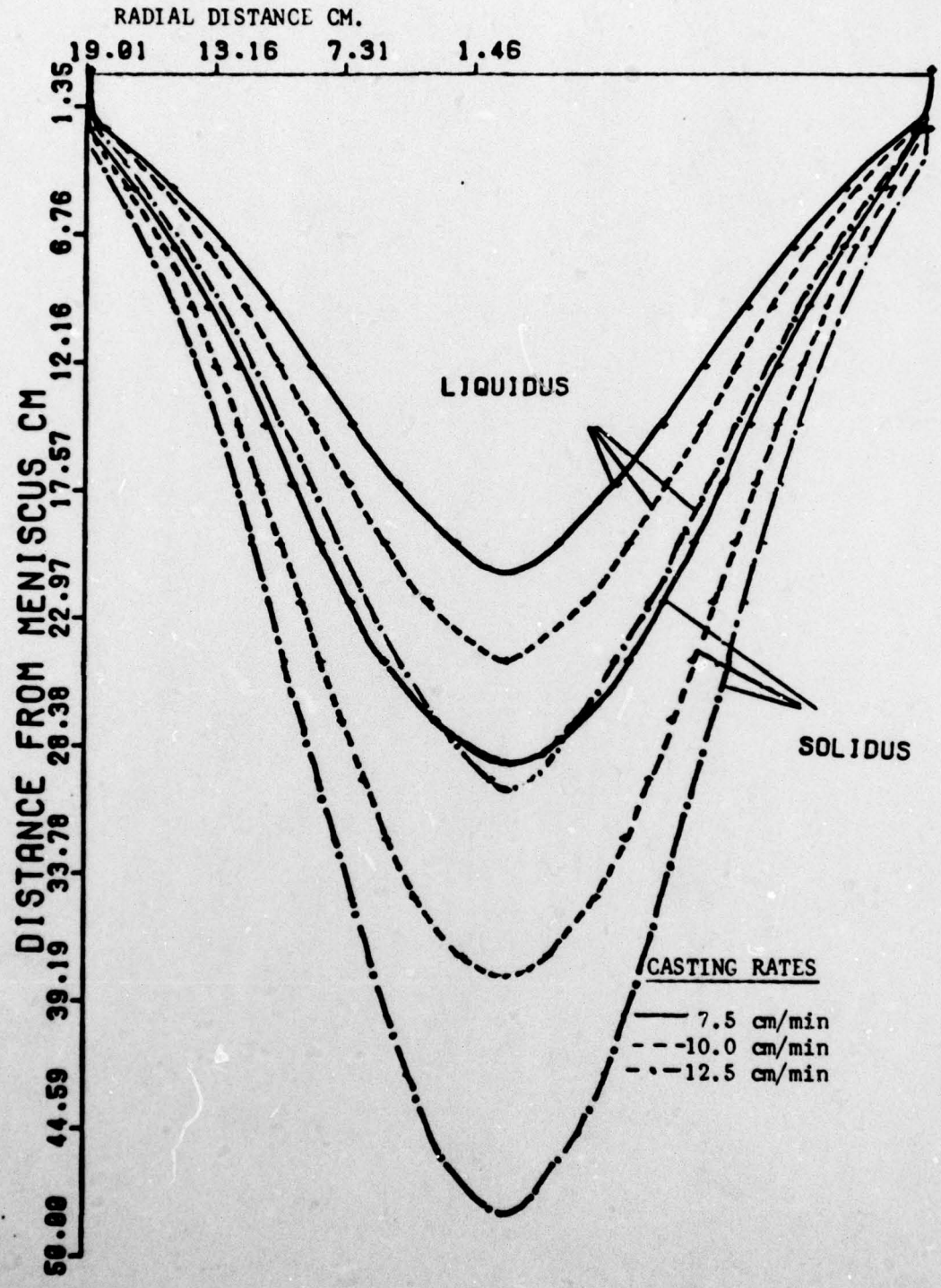

Figure 4 Effect of casting rate on the freezing profile in a 38 cm diameter 5082 Al-Mg alloy ingot cast at 7.5, 10 and 12.5 cm/min.